

# 3D thermoelastic solids under non-linear interface thermal and orthotropic frictional contact conditions

Iván Ubero-Martínez<sup>1</sup>  | Luis Rodríguez-Tembleque<sup>2</sup> | Jaime Cifuentes-Rodríguez<sup>1</sup> | José Vallepuga-Espinosa<sup>1</sup>

<sup>1</sup>Departamento de Tecnología Minera, Topográfica y de Estructuras, Universidad de León, León, Spain

<sup>2</sup>Escuela Técnica Superior de Ingeniería, Universidad de Sevilla, Sevilla, Spain

## Correspondence

Iván Ubero-Martínez, Departamento de Tecnología Minera, Topográfica y de Estructuras, Universidad de León, Campus de Vegazana s/n, 24071 León, Spain.

Email: [iubem@unileon.es](mailto:iubem@unileon.es)

Luis Rodríguez-Tembleque, Escuela Técnica Superior de Ingeniería, Universidad de Sevilla, Camino de los Descubrimientos s/n, 41092 Sevilla, Spain.  
Email: [luisroteso@us.es](mailto:luisroteso@us.es)

## Abstract

This article presents a robust and efficient methodology to study three-dimensional thermoelastic contact problems under orthotropic friction conditions, including the effects of non-linear thermal contact conductance and convective boundary conditions at the interstitial contact zone. The proposed methodology considers the boundary element method to compute the thermo-mechanical influence coefficients and an augmented Lagrangian formulation to ensure the fulfillment of all these thermomechanical contact conditions. The resulting non-linear equation set have been solved by an efficient proposed iterative Uzawa scheme. The proposed formulation has been validated by comparison with some available results in the literature and later on, it is considered to study how the thermoelastic contact variables are affected by both: the non-linear interface thermal and the orthotropic friction conditions in different engineering problems such as a brake disc-pad contact system.

## KEYWORDS

boundary element method, frictional contact, frictional heating, interstitial convective conditions, orthotropic friction, thermomechanical contact

## 1 | INTRODUCTION

Contact problems are clearly affected by the thermoelastic response of solids in contact. For instance, thermal loads or temperature variations in two solids in contact produce thermal tractions that can change the contact conditions and the contact zone due to the thermal distortion produced at the common interface. This thermal distortion affects not only a non-uniform normal traction and temperature distributions, as well as to the non-contact regions. Moreover, in engineering problems such as the design of machine components, it is also the great importance to consider effects from frictional heating. In many contact problems, the friction properties are not dependent on the sliding direction, so friction is assumed to be constant and modeled using the isotropic Coulomb law. However, in many engineering applications, the distribution of the surface asperities and hollows are not identical in every point of the surface. Thus, for this kind of cases, an anisotropic friction model has to be considered, obtaining a most realist frictional behavior. All of these leads to an increase of the inherent non-linearity of the problem since the temperature field along the contact zone depends on the pressure values and tangential displacements. So it is of great importance the approximation of the tangential contact variables during the resolution process due to the difficulties involved in fulfilling the anisotropic friction law.

In the literature, it is possible to find different works which studied and developed different frictional models such as References 1-5. Analytical solutions for some isotropic are presented in References 6,7. Moreover, other works on the literature such as References 8-11 present a numerical formulations for orthotropic frictional contact problems.

This is an open access article under the terms of the Creative Commons Attribution License, which permits use, distribution and reproduction in any medium, provided the original work is properly cited.

© 2022 The Authors. *International Journal for Numerical Methods in Engineering* published by John Wiley & Sons Ltd.

It is well known that contact problems involving friction are the most difficult ones to be solved in engineering, especially when considering more realistic friction models such as the one used in this work. A wide range of works of finite element method (FEM) based on contact problems may be found in the literature: it has to be mentioned the works of Wriggers et al.,<sup>12-14</sup> Johansson et al.,<sup>15</sup> Strömberg et al.,<sup>16-20</sup> Patunso,<sup>21</sup> Hüeber and Wohlmuth,<sup>22</sup> and Seitz et al.<sup>23</sup> in which thermomechanical contact problems with friction and/or wear are studied.

The boundary element method (BEM) has been also recognized by its numerical suitability on three dimensional interface interaction problems.<sup>24</sup> Therefore, the BEM has been used to studied the thermomechanical contact problems in different works such as References 25-35. Nevertheless, to the best author's knowledge, the inclusion of the orthotropic frictional law has been solved in References 36-42 for the resolution of contact problems using BEM for elastic, multifield magneto-electro-elastic and piezoelectric conditions, FRP composites and wear. Only in References 27,43,44 has been involved the isotropic friction model in 2D thermomechanical contact problems.

In this context, this work presents a numerical formulation to solve three-dimensional thermoelastic contact problems under frictional contact conditions. Contrary to what previous works assume, in this work are considered the frictional heating effects and an orthotropic frictional law. Additionally, non-linear thermal interface and interstitial convective conditions are also simulated. So, to the best authors' knowledge, it is the first time that a 3D thermoelastic contact formulation considers both, non-linear interface thermal and orthotropic frictional contact conditions, simultaneously. The thermomechanical influence coefficients are computed by means of the boundary element technique, whereas the augmented Lagrangian formulation<sup>45-48</sup> has been used to the contact modeling. Finally, the derived thermoelastic contact problem is solved using an Uzawa iterative scheme<sup>46,49-51</sup> which has been reformulated to consider the previous described nonlinear interface thermoelastic contact conditions.

The article is organized as follows: the basic governing equations are presented in Section 2. The non-linear thermoelastic contact conditions, including the anisotropic frictional law is presented in Section 3. In Section 4, a short description of the boundary element discrete equations and the solution procedure is presented. Section 5 is dedicated to the validation of the proposed formulation by comparison with benchmark problems. Moreover, additional engineering problems are also presented and discussed in detail in this section. Finally, the article concludes with the summary and the concluding remarks.

## 2 | GOVERNING EQUATIONS

Let consider two 3D isotropic bodies occupying each one the region  $\Omega^l \subset \mathbb{R}^3$  ( $l = A, B$ ) with a piecewise smooth boundary  $\Gamma^l$ , in a Cartesian coordinate system  $(x_1, x_2, x_3)$  (see Figure 1). Both bodies are under quasi-static thermoelastic contact conditions. The boundary  $\Gamma^l$  is divided in two different parts to define the mechanical and the thermal boundary conditions. The first one divides  $\Gamma^l$  into two separations:  $\Gamma^l = \Gamma_u^l \cup \Gamma_t^l$ , being the elastic displacements  $\bar{u}_i$  imposed on  $\Gamma_u^l$  and the traction  $\bar{t}_i$  prescribed on  $\Gamma_t^l$ . The second division is:  $\Gamma_\theta^l$  on which the temperature  $\bar{\theta}$  is prescribed,  $\Gamma_q^l$  with heat flux  $\bar{q}$  impose and  $\Gamma_{ic}^l$  which is defined as:  $\Gamma_{ic}^l = \Gamma_i^l \cup \Gamma_c$ , that is,  $\Gamma_c$  being the common contact zone and  $\Gamma_i^l$  being the interstitial region of each solid, that surrounds the contact zone, where convective heat transfer conditions are considered.

The thermomechanical equilibrium equations of the problem considering the absence of body forces are written as:

$$\begin{aligned} k_t \theta_{,ii} &= 0 \text{ in } \Omega^l, \\ \sigma_{ij,j} &= 0 \text{ in } \Omega^l, \end{aligned} \quad (1)$$

where  $k_t$  is the thermal conductivity,  $\theta$  is the temperature, and  $\sigma_{ij}$  are the components of Cauchy stress tensor. In this work, the summation convention is used.

The constitutive equation in  $\Omega^l$  for isotropic thermoelasticity can be written as:

$$\sigma_{ij} = \lambda \varepsilon_{kk} \delta_{ij} + 2\mu \varepsilon_{ij} - (3\lambda + 2\mu) \alpha_t (\theta - \theta_o) \delta_{ij}, \quad (2)$$

where  $\lambda$  and  $\mu$  are the Lamé coefficients,  $\alpha_t$  is the thermal dilatation coefficient,  $\theta_o$  is the reference temperature, and  $\varepsilon_{ij}$  is the infinitesimal strain tensor defined by

$$\varepsilon_{ij} = (u_{i,j} + u_{j,i})/2 \text{ in } \Omega^l. \quad (3)$$

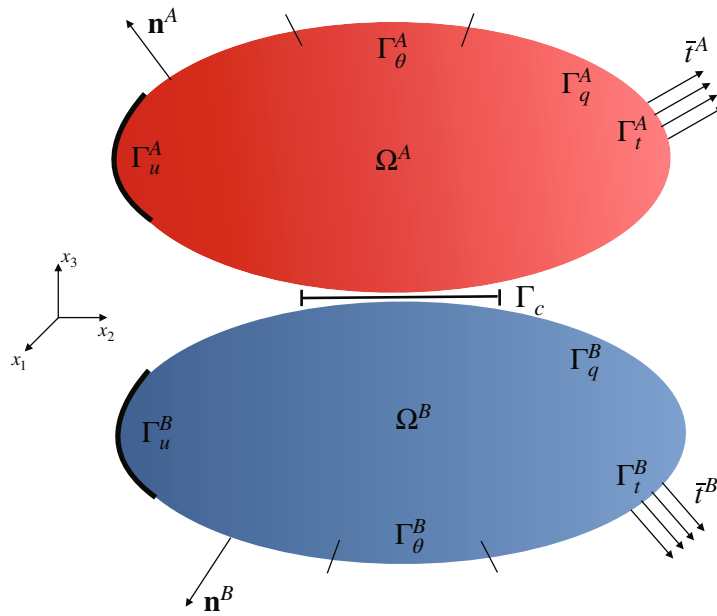


FIGURE 1 The physical setting

Prescribing thermal and mechanical boundary conditions on  $\Gamma^l$ . The Dirichlet boundary conditions are

$$\begin{aligned} \theta &= \bar{\theta} \text{ on } \Gamma_\theta^l, \\ u_i &= \bar{u}_i \text{ on } \Gamma_u^l. \end{aligned} \tag{4}$$

and the Neumann boundary conditions are given by

$$\begin{aligned} q &= \bar{q} \text{ on } \Gamma_q^l, \\ \sigma_{ij}n_j &= \bar{t}_i \text{ on } \Gamma_t^l. \end{aligned} \tag{5}$$

with  $\mathbf{n}$  being the outward unit normal to the boundary (see Figure 1) and the heat flux  $q$  is defined as  $q = q_i n_i$ , being  $q_i = -k_i \theta_{,i}$ .

For a well-posed problem either tractions or displacements and either temperatures or heat fluxes must be prescribed at each boundary zone outside  $\Gamma_{ic}^l$ . However, special considerations should be taken into account for the boundary conditions on  $\Gamma_{ic}^l$ .

On the interstitial region  $\Gamma_i^l$  a heat interchange between the bodies due to a fluid contained in the separation zones between them is considered. So the boundary

$$\begin{aligned} q &= \tilde{q}_i \text{ on } \Gamma_i^l, \\ \sigma_{ij}n_j &= \bar{t}_i \text{ on } \Gamma_i^l, \end{aligned} \tag{6}$$

where  $\mathbf{n}$  being the outward unit normal to the boundary (see Figure 1) and  $\tilde{q}_i$  depends on whether convective boundary conditions are considered, that is,  $\tilde{q}_i = h_f(\theta - \theta_f)$ . On these expressions, “ $h_f$ ” is the convection coefficient. On the other hand, it should be mentioned that the examples solved on this work assume  $\sigma_{ij}n_j = 0$  on  $\Gamma_i^l$ .

### 3 | THERMOMECHANICAL CONTACT CONDITIONS

#### 3.1 | Mechanical contact conditions

Assuming small displacements assumption, a common normal unit normal vector  $\mathbf{n}_c = (\mathbf{n}_3^A - \mathbf{n}_3^B) / \|\mathbf{n}_3^A - \mathbf{n}_3^B\|$  is calculated on the common contact area  $\Gamma_c$  (see Figure 2). Thus the nonlinear mechanical boundary conditions on  $\Gamma_c$  can be determined as

$$\sigma_{ij}n_{cj} = p_i \text{ on } \Gamma_c, \tag{7}$$

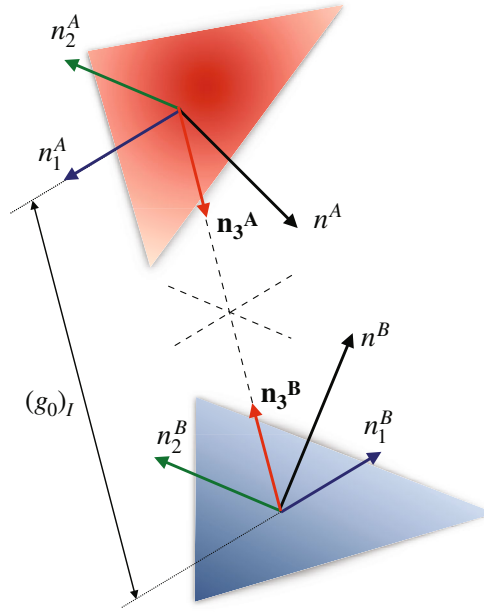


FIGURE 2 Local coordinate system for each contact pair of elements

where  $p_i$  is the contact traction. Assuming no friction contact conditions, the contact traction  $p_i$  has to satisfy the Signorini's conditions on  $\Gamma_c$ :

$$g_n \geq 0, p_n \leq 0, g_n p_n = 0, \tag{8}$$

where  $p_n = \mathbf{p} \cdot \mathbf{n}_c$  and  $g_n = (g_0 + u_n)$ , being  $g_0 = (\mathbf{x}^A - \mathbf{x}^B) \cdot \mathbf{n}_c$  the initial gap between the bodies (see Figure 2) and  $u_n = (\mathbf{u}^A - \mathbf{u}^B) \cdot \mathbf{n}_c$  is the relative displacement.

These normal contact constrains (8) can be reformulated in a more compact form as:

$$p_n - \mathbb{P}_{\mathbb{R}_-}(p_n^*) = 0, \tag{9}$$

where  $\mathbb{P}_{\mathbb{R}_-}(\cdot)$  is the normal projection function ( $\mathbb{P}_{\mathbb{R}_-}(\cdot) = \min(0, \cdot)$ ),  $p_n^* = p_n + r_n g_n$  is the augmented normal traction, where  $r_n$  is a penalization parameter ( $r_n \in \mathbb{R}^+$ ).

An orthotropic friction law<sup>37,51</sup> is considered, which is a more appropriate frictional constitutive law. The generic form of such orthotropic *Friction Cone* ( $\mathbb{C}_f$ ) is given by

$$f(\mathbf{p}_t, p_n) = \|\mathbf{p}_t\|_\mu - |p_n| = 0, \tag{10}$$

where  $\mathbf{p}_t = \mathbf{p} - p_n \mathbf{n}_c$  and  $\|\bullet\|_\mu$  denotes the elliptic norm

$$\|\mathbf{p}_t\|_\mu = \sqrt{(p_{e_1}/\mu_1)^2 + (p_{e_2}/\mu_2)^2}, \tag{11}$$

being  $\mu_1$  and  $\mu_2$  the principal friction coefficients in the directions  $\{e_1, e_2\}$ .

The Coulomb friction restriction ( $\|\mathbf{p}_t\|_\mu \leq |p_n|$ ) can be summarized as:

$$\begin{aligned} \|\mathbf{p}_t\|_\mu < |p_n| &\Rightarrow \dot{\mathbf{g}}_t = \mathbf{0} \text{ on } \Gamma_c, \\ \|\mathbf{p}_t\|_\mu = |p_n| &\Rightarrow \mathbf{p}_t = -|p_n| \mathbb{M}^2 \dot{\mathbf{g}}_t / \|\dot{\mathbf{g}}_t\|_\mu^* \text{ on } \Gamma_c, \end{aligned} \tag{12}$$

In the expressions above, the tangential slip velocity ( $\dot{\mathbf{g}}_t = \mathbf{v}_t$ ), whose module is defined as  $v_s = \|\dot{\mathbf{g}}_t\|$ , can be assumed for quasistatic contact problems as  $\dot{\mathbf{g}}_t \approx \Delta \mathbf{g}_t = \mathbf{g}_{0,\tau} - \mathbf{u}_t$  (i.e.,  $\mathbf{g}_{0,\tau}$  is the tangential translation and  $\mathbf{u}_t = \mathbf{u} - u_n \mathbf{n}_c$ ). In Equation

(12), the value for the tangential contact traction was presented in Reference 37 assuming an associated sliding rule, the norm  $\|\bullet\|_\mu^*$  is dual of  $\|\bullet\|_\mu$

$$\|\dot{\mathbf{g}}_t\|_\mu^* = \sqrt{(\mu_1 \dot{g}_{e_1})^2 + (\mu_2 \dot{g}_{e_2})^2}, \quad (13)$$

and  $\mathbb{M}$  is a diagonal matrix:

$$\mathbb{M} = \begin{bmatrix} \mu_1 & 0 \\ 0 & \mu_2 \end{bmatrix}. \quad (14)$$

The frictional contact constraints (12) can be also formulated using contact operators as:

$$\mathbf{p}_t - \mathbb{P}_{\mathbb{E}_\rho}(\mathbf{p}_t^*) = 0, \quad (15)$$

where  $\mathbf{p}_t^* = \mathbf{p}_t - r_t \mathbb{M}^2 \dot{\mathbf{g}}_t$  ( $r_t \in \mathbb{R}^+$ ) is the augmented tangential traction and  $\mathbb{P}_{\mathbb{E}_\rho}(\bullet) : \mathbb{R}^2 \rightarrow \mathbb{R}^2$  is the tangential projection function defined in Reference 37 as

$$\mathbb{P}_{\mathbb{E}_\rho}(\mathbf{p}_t^*) = \begin{cases} \mathbf{p}_t^* & \text{if } \|\mathbf{p}_t^*\|_\mu < \rho, \\ \rho \mathbf{p}_t^* / \|\mathbf{p}_t^*\|_\mu & \text{if } \|\mathbf{p}_t^*\|_\mu \geq \rho, \end{cases} \quad (16)$$

with  $\rho = |\mathbb{P}_{\mathbb{R}_-}(p_n^*)|$ .

### 3.2 | Thermal contact conditions

The thermal interface contact conditions are derived, according to References 16,19, from the general energy balance of the contact interface in assumption of zero heat capacity of the interfaces and orthotropic friction (10). So the energy balance for the contact interface can be written as

$$q^A + q^B + |p_n| \|\dot{\mathbf{g}}_t\|_\mu^* = 0, \quad (17)$$

where the heat fluxes are given by:

$$q^A = \varphi_A(\theta^A - \theta_o), \quad q^B = \varphi_B(\theta^B - \theta_o). \quad (18)$$

In the expression above,  $\varphi_l$  ( $l = A, B$ ) represents the thermal contact conductance and  $\theta_o$  is the intrinsic temperature of  $\Gamma_c$ . From Equations (17) and (18) it is possible to obtain the intrinsic temperature

$$\theta_o = \frac{\varphi_A \theta^A + \varphi_B \theta^B}{\varphi_A + \varphi_B} + \frac{1}{\varphi_A + \varphi_B} |p_n| \|\dot{\mathbf{g}}_t\|_\mu^*. \quad (19)$$

Thus, the expression for the heat fluxes becomes:

$$q^A = \varphi_o(\theta^A - \theta^B) - \xi_\mu^A |p_n| \|\dot{\mathbf{g}}_t\|_\mu^*, \quad (20)$$

$$q^B = \varphi_o(\theta^B - \theta^A) - \xi_\mu^B |p_n| \|\dot{\mathbf{g}}_t\|_\mu^*, \quad (21)$$

where  $\varphi_o = \varphi_A \varphi_B / (\varphi_A + \varphi_B)$  represents the overall contact conductance and  $\xi_\mu^l = \varphi_l / (\varphi_A + \varphi_B)$  ( $l = A, B$ ) represents factors on how frictional dissipation is divided between the contact interface and the contact surfaces, respectively, being  $\xi_\mu^A + \xi_\mu^B = 1$ .

### 3.3 | Thermal contact conductance

The overall thermal contact conductance of two rough surfaces in contact (see Figure 3), can be calculated as:

$$\varphi_o = \varphi_c + \varphi_g, \quad (22)$$

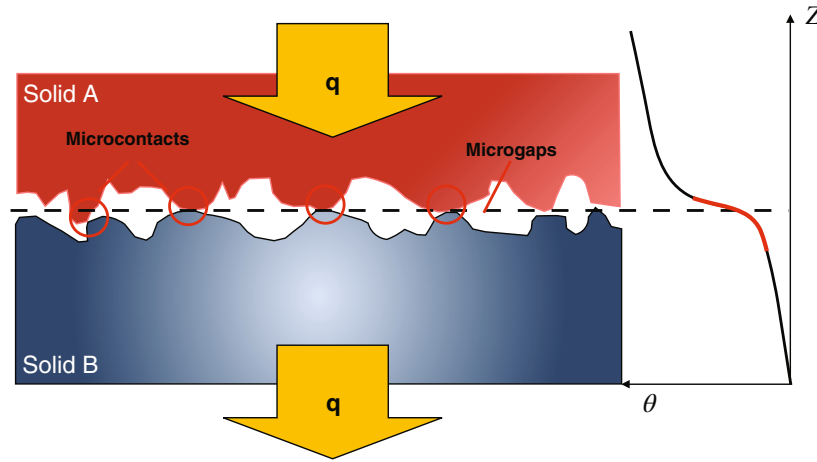


FIGURE 3 General thermal contact model and the schematic contact temperature distribution along the two solids contact surfaces

where  $\varphi_c$  and  $\varphi_g$  are, respectively, the contact and microgap conductance. Thus,  $\varphi_o(p_n) = \varphi_c + \varphi_g$  in Equations (20) and (21).

The contact conductance depends on different geometric, thermal and mechanical parameters.<sup>52-55</sup> Based on works,<sup>52-55</sup> the general form of the contact conductance can be written as:

$$\varphi_c = 1.25 \cdot k_c \frac{m_c}{\sigma_c} \left( \frac{|p_n|}{H_c} \right)^{0.95}, \quad (23)$$

where,  $k_c = 2k^A k^B / (k^A + k^B)$  is the harmonic mean thermal conductivity of the interface.  $H_c = 2H^A H^B / (H^A + H^B)$  defines the contact microhardness,  $\sigma_c = \sqrt{(\sigma^A)^2 + (\sigma^B)^2}$  is the effective joint surface roughness. Finally,  $m_c = \sqrt{(m^A)^2 + (m^B)^2}$  represents the effective mean absolute asperity slope.

However, the heat flows from one solid to the other not only by means of conduction through the microcontacts but also by the microgaps when they are filled with a thermal interface material (TIM). For that reason,  $\varphi_g$  is defined, according to Reference 54 as:

$$\varphi_g = \frac{k_g}{Y}, \quad (24)$$

where  $k_g$  is the TIM thermal conductivity and  $Y$  is the mean plane separation which depends on the normal contact pressure.<sup>54</sup>  $Y$  can be written as:

$$Y = 1.363 \sigma_c \left[ -\ln \left( 5.589 \frac{p_n}{H_c} \right) \right]^{0.5}. \quad (25)$$

### 3.4 | Interstitial thermal conditions

A heat exchange between both solids is assumed on the interstitial region  $\Gamma_i^l$  by containing a fluid in the separation zones. The heat interchange is produced by means of convective conditions. These convective conditions are divided in two: forced convection and natural convection conditions.

For the case of forced convection conditions, the following boundary conditions are applied:

$$q^l = h_f (\theta_f - \theta^l), \quad (26)$$

being  $h_f$  the convection coefficient and  $\theta_f$  the fluid temperature. However, if natural convective conditions are considered, the thermal conditions are obtained according to References 26,31,56 and are given by:

$$q^B(\alpha) = -q^A(\alpha), \quad (27)$$

$$q^A(\alpha) = \varphi_o(\theta^B(\alpha) - \theta^A(\alpha)), \quad (28)$$

where  $\varphi_o$  is a pseudo-conductance with value  $h_f/2$ .

## 4 | BOUNDARY ELEMENT FORMULATION

### 4.1 | Boundary element equations

The well-known steady-state boundary integral equations for thermoelastic problems can be presented, according to Aliabadi,<sup>24</sup> as follows. First, the temperature integral equation of collocation point  $\mathbf{X}$  on  $\Gamma^i$ :

$$c(\mathbf{X})\theta(\mathbf{X}) + \int_{\Gamma} Q(\mathbf{x}, \mathbf{X})\theta(\mathbf{x}) d\Gamma(\mathbf{x}) = \int_{\Gamma} \Theta(\mathbf{x}, \mathbf{X})q(\mathbf{x}) d\Gamma(\mathbf{x}), \tag{29}$$

where  $\mathbf{x}$  is a boundary point,  $c(\mathbf{X})$  are the free term of the temperature boundary integral equation and  $Q(\mathbf{x}, \mathbf{X})$  and  $\Theta(\mathbf{x}, \mathbf{X})$  are the fundamental solutions of the thermal problem. And second, the displacement integral equation

$$\begin{aligned} c_{ij}(\mathbf{X})u_j(\mathbf{X}) - \int_{\Gamma} U_{ij}(\mathbf{x}, \mathbf{X})t_j(\mathbf{x}) d\Gamma(\mathbf{x}) + \int_{\Gamma} T_{ij}(\mathbf{x}, \mathbf{X})u_j(\mathbf{x}) d\Gamma(\mathbf{x}) \\ = \int_{\Gamma} \bar{Q}_i(\mathbf{x}, \mathbf{X})\theta(\mathbf{x}) d\Gamma(\mathbf{x}) - \int_{\Gamma} \bar{\Theta}_i(\mathbf{x}, \mathbf{X})q(\mathbf{x}) d\Gamma(\mathbf{x}), \end{aligned} \tag{30}$$

where  $\mathbf{x}$  is a boundary point,  $c_{ij}(\mathbf{X})$  is the free terms of the boundary integral equations for the elastic problem.  $T_{ij}(\mathbf{x}, \mathbf{X})$  stands for the tractions fundamental solution and  $U_{ij}(\mathbf{x}, \mathbf{X})$  is the fundamental solution tensor for displacement. Finally,  $\bar{Q}_i(\mathbf{x}, \mathbf{X})$  and  $\bar{\Theta}_i(\mathbf{x}, \mathbf{X})$  are the vectors derived from the consideration of thermal deformations in the elastic law.

After discretizing the boundary, Equations (29) and (30) can be regrouped and written as  $\mathbf{H}\tilde{\mathbf{u}} = \mathbf{G}\tilde{\mathbf{t}}$ .  $\tilde{\mathbf{u}}$  gathers the values of all nodal displacements ( $\mathbf{u}$ ) and temperature ( $\theta$ ) vectors, and  $\tilde{\mathbf{t}}$  contains the nodal tractions ( $\mathbf{t}$ ) and the nodal heat fluxes ( $\mathbf{q}$ ) vectors. Applying the boundary conditions, the previous expression can be written as:  $\mathbf{A}\tilde{\mathbf{x}} = \mathbf{F}$ , where all the unknowns are passed to the left-hand side vector  $\tilde{\mathbf{x}}$ .

Considering node to node contact, the interface discretization on  $\Gamma_c$  implemented for contact problems. Thus, each node on  $\Gamma_c^l$  makes a contact pair ( $l$ ). Therefore, the respective boundary element equation  $\mathbf{A}^l\tilde{\mathbf{x}}^l = \mathbf{F}^l$  for the solid  $\Omega^l$  ( $l = A, B$ ) can be expressed as:

$$\mathbf{A}_{x_e}^l \mathbf{x}_e^l + \mathbf{A}_{u_c}^l \mathbf{u}_c^l + \mathbf{A}_{\theta_c}^l \theta_c^l + \mathbf{A}_p^l \mathbf{p}_c^l + \mathbf{A}_q^l \mathbf{q}_c^l = \mathbf{F}^l, \tag{31}$$

where  $(\mathbf{x}^l)^T = [(\mathbf{x}_e^l)^T (\mathbf{u}_c^l)^T (\theta_c^l)^T]$  is a vector with the nodal unknowns in which:

- $(\mathbf{x}_e^l)$  gathers the external unknowns.
- $(\mathbf{u}_c^l)$  includes the contact displacements.
- $(\theta_c^l)$  correspond to the contact temperatures.

Matrix  $\mathbf{A}_x^l$  is formed with the column of matrices  $\mathbf{H}^l$  and  $\mathbf{G}^l$ , and  $\mathbf{A}_p^l$  and  $\mathbf{A}_q^l$  is assembled with the columns of  $\mathbf{G}^l$  that belong to the contact nodal unknowns. Thus, for contact problems, the discrete boundary element equation (31) for the solids in contact can be organized as:

$$\begin{bmatrix} \mathbf{A}_{x_e}^A & \mathbf{0} & \mathbf{A}_{u_c}^A & \mathbf{0} & \mathbf{A}_{\theta_c}^A & \mathbf{0} & \mathbf{A}_{p_c}^A & \mathbf{A}_q^A & \mathbf{0} \\ \mathbf{0} & \mathbf{A}_{x_e}^B & \mathbf{0} & \mathbf{A}_{u_c}^B & \mathbf{0} & \mathbf{A}_{\theta_c}^B & -\mathbf{A}_{p_c}^B & \mathbf{0} & \mathbf{A}_q^B \end{bmatrix} \begin{Bmatrix} \mathbf{x}_e^A \\ \mathbf{x}_e^B \\ \mathbf{u}_c^A \\ \mathbf{u}_c^B \\ \theta_c^A \\ \theta_c^B \\ \mathbf{p}_c \\ \mathbf{q}_c^A \\ \mathbf{q}_c^B \end{Bmatrix} = \begin{Bmatrix} \mathbf{F}^A \\ \mathbf{F}^B \end{Bmatrix}, \tag{32}$$

In the above expression, the normal contact tractions vector of every pair of nodes ( $I$ ) are gathered in vector  $\mathbf{p}_c$ . They are respectively related with the nodal boundary element tractions and heat flux vectors among the equilibrium equation:  $(\mathbf{p}_c)_I = (\mathbf{p}_c^A)_I = -(\mathbf{p}_c^B)_I$ .

The boundary element equation (32) can be reordered in a more compact form:

$$\begin{bmatrix} \mathbf{A}_{x_e} & \mathbf{A}_{u_c} & \mathbf{A}_{\theta_c} & \mathbf{A}_{p_c} & \mathbf{A}_{q_c} \end{bmatrix} \begin{Bmatrix} \mathbf{x}_e \\ \mathbf{u}_c \\ \theta_c \\ \mathbf{p}_c \\ \mathbf{q}_c \end{Bmatrix} = \mathbf{F}, \quad (33)$$

where  $\mathbf{x}_e$  collects the nodal external unknowns (i.e., the nodal unknowns which are outside the contact zone),  $\mathbf{u}_c$  and  $\theta_c$  collect the nodal contact displacements and temperatures, respectively,  $\mathbf{p}_c$  contains the nodal contact tractions and  $\mathbf{q}_c$  contains the nodal contact heat fluxes on each solid:

$$\mathbf{x}_e = \begin{Bmatrix} \mathbf{x}_e^A \\ \mathbf{x}_e^B \end{Bmatrix}, \quad \mathbf{u}_c = \begin{Bmatrix} \mathbf{u}_c^A \\ \mathbf{u}_c^B \end{Bmatrix}, \quad \theta_c = \begin{Bmatrix} \theta_c^A \\ \theta_c^B \end{Bmatrix}, \quad \mathbf{q}_c = \begin{Bmatrix} \mathbf{q}_c^A \\ \mathbf{q}_c^B \end{Bmatrix}. \quad (34)$$

Matrices  $\mathbf{A}_{x_e}$ ,  $\mathbf{A}_{u_c}$ ,  $\mathbf{A}_{\theta_c}$ ,  $\mathbf{A}_{p_c}$ , and  $\mathbf{A}_{q_c}$ , and vector  $\mathbf{F}$  are constructed as:

$$\mathbf{A}_{x_e} = \begin{bmatrix} \mathbf{A}_{x_e}^A & \mathbf{0} \\ \mathbf{0} & \mathbf{A}_{x_e}^B \end{bmatrix}, \quad \mathbf{A}_{u_c} = \begin{bmatrix} \mathbf{A}_{u_c}^A & \mathbf{0} \\ \mathbf{0} & \mathbf{A}_{u_c}^B \end{bmatrix}, \quad \mathbf{A}_{\theta_c} = \begin{bmatrix} \mathbf{A}_{\theta_c}^A & \mathbf{0} \\ \mathbf{0} & \mathbf{A}_{\theta_c}^B \end{bmatrix}, \quad (35)$$

$$\mathbf{A}_{p_c} = \begin{bmatrix} \mathbf{A}_{p_c}^A \\ -\mathbf{A}_{p_c}^B \end{bmatrix}, \quad \mathbf{A}_q = \begin{bmatrix} \mathbf{A}_q^A & \mathbf{0} \\ \mathbf{0} & \mathbf{A}_q^B \end{bmatrix}, \quad \mathbf{F} = \begin{Bmatrix} \mathbf{F}^A \\ \mathbf{F}^B \end{Bmatrix}. \quad (36)$$

## 4.2 | Thermoelastic contact discrete variables and restrictions

For every contact pair on nodes ( $I$ ), the heat flux can be calculated in terms of the thermal contact conductance ( $\varphi_o$ ) and the temperature of every solid, according to (20) and (21), as:

$$(\mathbf{q}_c^A)_I = \varphi_o((\mathbf{p}_n)_I) ((\theta^A)_I - (\theta^B)_I) - \xi_\mu^A |(\mathbf{p}_n)_I| \|(\dot{\mathbf{g}}_t)_I\|_\mu^*, \quad (37)$$

$$(\mathbf{q}_c^B)_I = \varphi_o((\mathbf{p}_n)_I) ((\theta^B)_I - (\theta^A)_I) - (1 - \xi_\mu^A) |(\mathbf{p}_n)_I| \|(\dot{\mathbf{g}}_t)_I\|_\mu^*, \quad (38)$$

where  $\mathbf{p}_n$  contains the normal contact pressures.

So Equation (33) can be written as

$$\begin{bmatrix} \mathbf{A}_{x_e} & \mathbf{A}_{u_c} & \tilde{\mathbf{A}}_{\theta_c} & \mathbf{A}_{p_c} \end{bmatrix} \begin{Bmatrix} \mathbf{x}_e \\ \mathbf{u}_c \\ \theta_c \\ \mathbf{p}_c \end{Bmatrix} = \tilde{\mathbf{F}}, \quad (39)$$

where

$$\tilde{\mathbf{A}}_{\theta_c} = \begin{bmatrix} \mathbf{A}_{\theta_c}^A + \varphi_o(\mathbf{p}_n)\mathbf{A}_q^A & -\varphi_o(\mathbf{p}_n)\mathbf{A}_q^A \\ -\varphi_o(\mathbf{p}_n)\mathbf{A}_q^B & \mathbf{A}_{\theta_c}^B + \varphi_o(\mathbf{p}_n)\mathbf{A}_q^B \end{bmatrix}, \quad \tilde{\mathbf{F}} = \begin{Bmatrix} \mathbf{F}^A + \xi_\mu^A \mathbf{A}_q^A \xi(\mathbf{p}_n, \dot{\mathbf{g}}_t) \\ \mathbf{F}^B + (1 - \xi_\mu^A) \mathbf{A}_q^B \xi(\mathbf{p}_n, \dot{\mathbf{g}}_t) \end{Bmatrix}, \quad (40)$$

being  $\varphi_o(\mathbf{p}_n)$  a diagonal matrix, that is:

$$\varphi_o(\mathbf{p}_n) = \text{diag}(\varphi_o((\mathbf{p}_n)_1), \dots, \varphi_o((\mathbf{p}_n)_I), \dots, \varphi_o((\mathbf{p}_n)_{N_c})), \quad (41)$$



and

$$\xi(\mathbf{p}_n, \dot{\mathbf{g}}_t) = \left\{ \begin{array}{c} \vdots \\ |(\mathbf{p}_n)_I| \|\dot{\mathbf{g}}_t\|_\mu^* \\ \vdots \end{array} \right\}. \tag{42}$$

Finally, the mechanical contact restrictions (9) and (15) are defined on every contact pair  $I$  as:

$$(\mathbf{p}_n)_I - \mathbb{P}_{\mathbb{R}_-}((\mathbf{p}_n)_I + r_n(\mathbf{g}_n)_I) = 0, \tag{43}$$

$$(\mathbf{p}_t)_I - \mathbb{P}_{\mathbb{E}_\rho}((\mathbf{p}_t)_I - r_t \mathbb{M}^2(\dot{\mathbf{g}}_t)_I) = 0, \tag{44}$$

where  $\mathbf{p}_n$  and  $\mathbf{p}_t$  contain the normal and tangential contact tractions of every contact node  $I$ ,  $\mathbf{g}_n$  contain the normal gaps and  $\dot{\mathbf{g}}_t$  slip velocities.

The quasi-static thermoelastic contact problem presented in Sections 2 and 3 can now be numerically treated by using the Equations (39)–(44). So defining  $\mathbf{z} = (\mathbf{x}_e, \mathbf{u}_c, \theta_c, \mathbf{p}_c)$ , we have the following system of non-linear equations for each load step:

$$\mathbf{H}(\mathbf{z}) = \left\{ \begin{array}{c} \mathbf{A}_{x_e} \mathbf{x}_e + \mathbf{A}_{u_c} \mathbf{u}_c + \tilde{\mathbf{A}}_{\theta_c} \theta_c + \mathbf{A}_{p_c} \mathbf{p}_c - \tilde{\mathbf{F}} \\ \mathbf{p}_c - \mathbb{P}_{\mathbb{C}_f}(\mathbf{p}_c^*) \end{array} \right\} = \mathbf{0}, \tag{45}$$

where the contact operator  $\mathbb{P}_{\mathbb{C}_f}$  projects the nodal augmented contact tractions in to the *Friction Cone* ( $\mathbb{C}_f$ ):

$$\mathbb{P}_{\mathbb{C}_f}((\mathbf{p}_c^*)_I) = \left\{ \begin{array}{c} \mathbb{P}_{\mathbb{R}_-}((\mathbf{p}_n^*)_I) \\ \mathbb{P}_{\mathbb{E}_\rho}((\mathbf{p}_t^*)_I) \end{array} \right\}. \tag{46}$$

### 4.3 | Solution scheme

An iterative Uzawa’s method based on Reference 41 is used to solve the resulting nonlinear system (33)–(45). Similar solution schemes can be found in References 46,50,51,57. To calculate the variables on load step  $(k)$ ,  $\mathbf{z}^{(k)} = (\mathbf{x}_e^{(k)}, \mathbf{u}_c^{(k)}, \theta_c^{(k)}, \mathbf{p}_c^{(k)})$ , when the variables on previous instant  $\mathbf{z}^{(k-1)}$  are known:

- (I) Set  $\mathbf{z}^{(0)} = \mathbf{z}^{(k-1)}$  and iterate using  $(n)$  index.
- (II) Resolve:

$$\left[ \begin{array}{ccc} \mathbf{A}_{x_e} & \mathbf{A}_{u_c} & \tilde{\mathbf{A}}_{\theta_c}^{(n)} \end{array} \right] \left\{ \begin{array}{c} \mathbf{x}_e \\ \mathbf{u}_c \\ \theta_c \end{array} \right\}^{(n+1)} = -\mathbf{A}_{p_c} \mathbf{p}_c^{(n)} + \tilde{\mathbf{F}}^{(n)}, \tag{47}$$

where

$$\tilde{\mathbf{A}}_{\theta_c}^{(n)} = \left[ \begin{array}{cc} \mathbf{A}_{\theta_c}^A + \varphi_o(\mathbf{p}_n^{(n)}) \mathbf{A}_q^A & -\varphi_o(\mathbf{p}_n^{(n)}) \mathbf{A}_q^A \\ -\varphi_o(\mathbf{p}_n^{(n)}) \mathbf{A}_q^B & \mathbf{A}_{\theta_c}^B + \varphi_o(\mathbf{p}_n^{(n)}) \mathbf{A}_q^B \end{array} \right], \quad \tilde{\mathbf{F}}^{(n)} = \left\{ \begin{array}{c} \mathbf{F}^A + \xi_\mu^A \mathbf{A}_q^A \xi(\mathbf{p}_n^{(n)}, \dot{\mathbf{g}}_t^{(k)}) \\ \mathbf{F}^B + (1 - \xi_\mu^A) \mathbf{A}_q^B \xi(\mathbf{p}_n^{(n)}, \dot{\mathbf{g}}_t^{(k)}) \end{array} \right\}. \tag{48}$$

- (III) Update contact tractions for every contact node  $I$ :

$$(\mathbf{p}_n^{(n+1)})_I = \mathbb{P}_{\mathbb{R}_-}((\mathbf{p}_n^{(n)})_I + r_n(\mathbf{g}_n^{(n+1)})_I), \tag{49}$$

$$(\mathbf{p}_t^{(n+1)})_I = \mathbb{P}_{\mathbb{E}_\rho}((\mathbf{p}_t^{(n)})_I - r_t \mathbb{M}^2(\dot{\mathbf{g}}_t^{(k)})_I), \tag{50}$$

where  $(\mathbf{g}_n^{(n+1)})_I = (\mathbf{g}_o^{(k)})_I + ((\mathbf{u}_c^A)_I - (\mathbf{u}_c^B)_I^{(n)}) \cdot (\mathbf{n}_c)_I$  and  $\rho = |(\mathbf{p}_n^{(n+1)})_I|$ .

(IV) Calculate the error  $\Psi(\mathbf{z}^{(n+1)}) = \max\{\|\mathbf{u}_c^{(n+1)} - \mathbf{u}_c^{(n)}\|, \|\boldsymbol{\theta}_c^{(n+1)} - \boldsymbol{\theta}_c^{(n)}\|, \|\mathbf{p}_c^{(n+1)} - \mathbf{p}_c^{(n)}\|\}$ .

(a) If  $\Psi(\mathbf{z}^{(n+1)}) \leq \varepsilon$ , the solution for the instant ( $k$ ) is reached:  $\mathbf{z}^{(k)} = \mathbf{z}^{(n+1)}$ .

(b) Otherwise, return to (II) evaluating:  $\mathbf{p}_c^{(n)} = \mathbf{p}_c^{(n+1)}$ .

After the solution at instant ( $k$ ) is reached, the solution for the next instant is achieved by setting:  $\mathbf{z}^{(0)} = \mathbf{z}^{(k)}$  and returning to (I).

The stop criterion is the similar to the predictor-corrector Uzawa scheme for contact presented by Kikuchi and Oden<sup>49</sup> or Joli and Feng.<sup>10</sup> However, additional stop criterion based on the norm of violation of the relations describing the discretized problem can be considered (i.e.,  $\Psi(\mathbf{z}) \leq \varepsilon$  being  $\Psi(\mathbf{z}) = \mathbf{H}^T(\mathbf{z})\mathbf{H}(\mathbf{z})/2$ ).

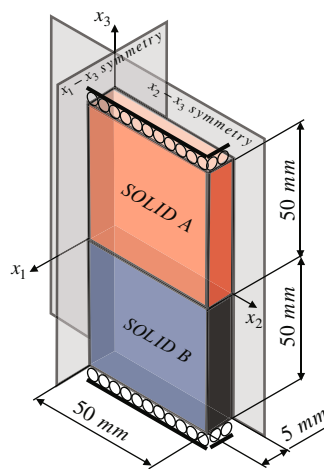
## 5 | NUMERICAL RESULTS

In order to show the capabilities of the proposed BEM formulation for 3D thermoelastic contact problems, some numerical results are presented in this section. First, the methodology is validated by comparison with numerical results presented in the literature,<sup>27</sup> in which different thermal resistance models are simulated. Then, the influence of frictional heating are demonstrated under different sliding directions ( $\beta$ ). Furthermore, the combined effects of the orthotropic friction law, the inclusion of a thermal interface material and interstitial convective conditions are analyzed. Finally, the thermomechanical contact variables are studied in a brake disc-pad contact system problem.

### 5.1 | Thermoelastic contact of two solids

In this first example, the methodology herein proposed is validated by comparison of the results obtained by solving the benchmark problem presented by Giannopoulos,<sup>27</sup> in which a 2D thermoelastic contact problem is solved. Giannopoulos<sup>27</sup> used a isotropic friction law with different friction coefficients ( $\mu = 0.1$ ,  $\mu = 0.2$ , and  $\mu = 0.3$ ). Thus, in order to compare the results herein obtained with the Giannopoulos ones, the following orthotropic friction coefficients have been used:  $\mu_1 = \mu_2 = 0.1$ ,  $\mu_1 = \mu_2 = 0.2$ , and  $\mu_1 = \mu_2 = 0.3$ . The geometry of the two blocks is illustrated in Figure 4 and the employed materials parameters are collected in Table 1.

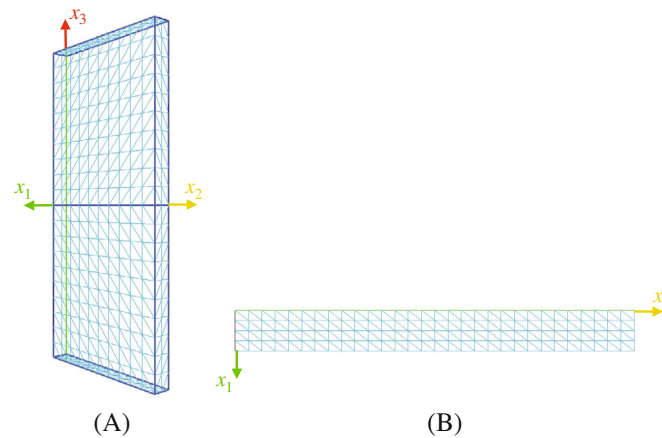
Symmetry conditions have been applied in planes  $x_1 - x_3$  and  $x_2 - x_3$ , so the faces corresponding to those planes have not been meshed. Figure 5 shows the meshing considered in this work. Both solids have been meshed with a total of 520 elements. The potential contact zone is discretized with 240 elements (see Figure 5B). The perpendicular displacements ( $u_{x_3} = 0$ ) are restricted in both upper face of the upper solid ( $x_3 = 50 \cdot 10^{-3}$  m) and lower face of the lower block ( $x_3 = -50 \cdot 10^{-3}$  m), whereas tractions are imposed ( $t_{x_1} = t_{x_2} = t_{x_3} = 0$ ) on the rest of the faces. Moreover, the upper face of the



**FIGURE 4** Geometry of a thermoelastic contact between two 3D rectangular solids considered for plane stress problem. Symmetry for planes  $x_1 - x_3$  and  $x_2 - x_3$  is applied

TABLE 1 Material parameters of the two solids

	Solid A	Solid B
E (GPa)	210	210
$\nu$	0.3	0.3
$\alpha$ ( $^{\circ}\text{C}^{-1}$ )	$2.25 \cdot 10^{-5}$	$1 \cdot 10^{-5}$
$k^l$ ( $\text{W}/^{\circ}\text{C mm}$ )	$60 \cdot 10^{-3}$	$40 \cdot 10^{-3}$
$\delta$ (mm/W)	$48.75 \cdot 10^{-5}$	$32.5 \cdot 10^{-6}$

FIGURE 5 (A) Boundary element mesh of the boundary of the 3D solids. (B) Boundary element mesh of the potential contact zone ( $\Gamma_c$ )

upper solid is with a constant temperature of  $\theta = 50^{\circ}\text{C}$  and the lower face of the upper block is with a constant temperature of  $\theta = -50^{\circ}\text{C}$ . On the rest of the faces, the heat flow is restricted,  $q = 0 \text{ W}/\text{mm}^2$ .

The formulation herein presented has been validate by considering and modeling the same thermal contact conductances as Reference 27:

- (a)  $\varphi_o = \infty$ ,
- (b)  $\varphi_o = \varphi_{01} = 0.0002^{0.01(p_n)}$  ( $\text{W}/^{\circ}\text{C m}^2$ ),
- (c)  $\varphi_o = \varphi_{02} = 0.002^{0.01(p_n)}$  ( $\text{W}/^{\circ}\text{C m}^2$ ),
- (d)  $\varphi_o = 0$ .

The thermal contact conductance presented in case (a) corresponds to an infinity thermal conductance model ( $\varphi_o = \infty$ ). Cases (b) and (c) represents intermediate conductances. Finally, case (d) simulates no heat transfer condition between the surfaces in contact ( $\varphi_o = 0$ ).

Figure 6 shows the normal contact traction distribution and the tangential traction distribution for the different thermal contact conductances simulated in Reference 27. The tractions values increases as the conductance ( $\varphi_o$ ) decreases. An excellent similarity between the numerical results obtained by the formulation proposed in this work and the results presented in the literature. The same agreement is showed in Figure 7, where the temperature distributions are plotted. A temperature jump in the contact zone is produced by the thermal contact conductance as it is shown in Figure 8.

On the one hand, Figure 9 shows the great influence of the thermal contact resistance on the value of pressures and temperatures in the contact zone. This relates to what is seen in Figures 6A and 7. As contact pressure increases, the thermal jump in the contact zone increases due to the decreased value of the thermal conductance ( $\varphi_o$ ).

Finally, after the validation with Giannopoulos,<sup>27</sup> where an isotropic friction law was considered, we are going to consider a scenario where orthotropic frictional contact conditions, that is,  $\mu_1 = 0.3$  and  $\mu_2 = 0.1$  (and vice versa), and different thermal contact conductance values are considered. The results for this study are presented in Figure 10, where the tangential tractions computed on each case are in comparison with the corresponding isotropic friction cases.

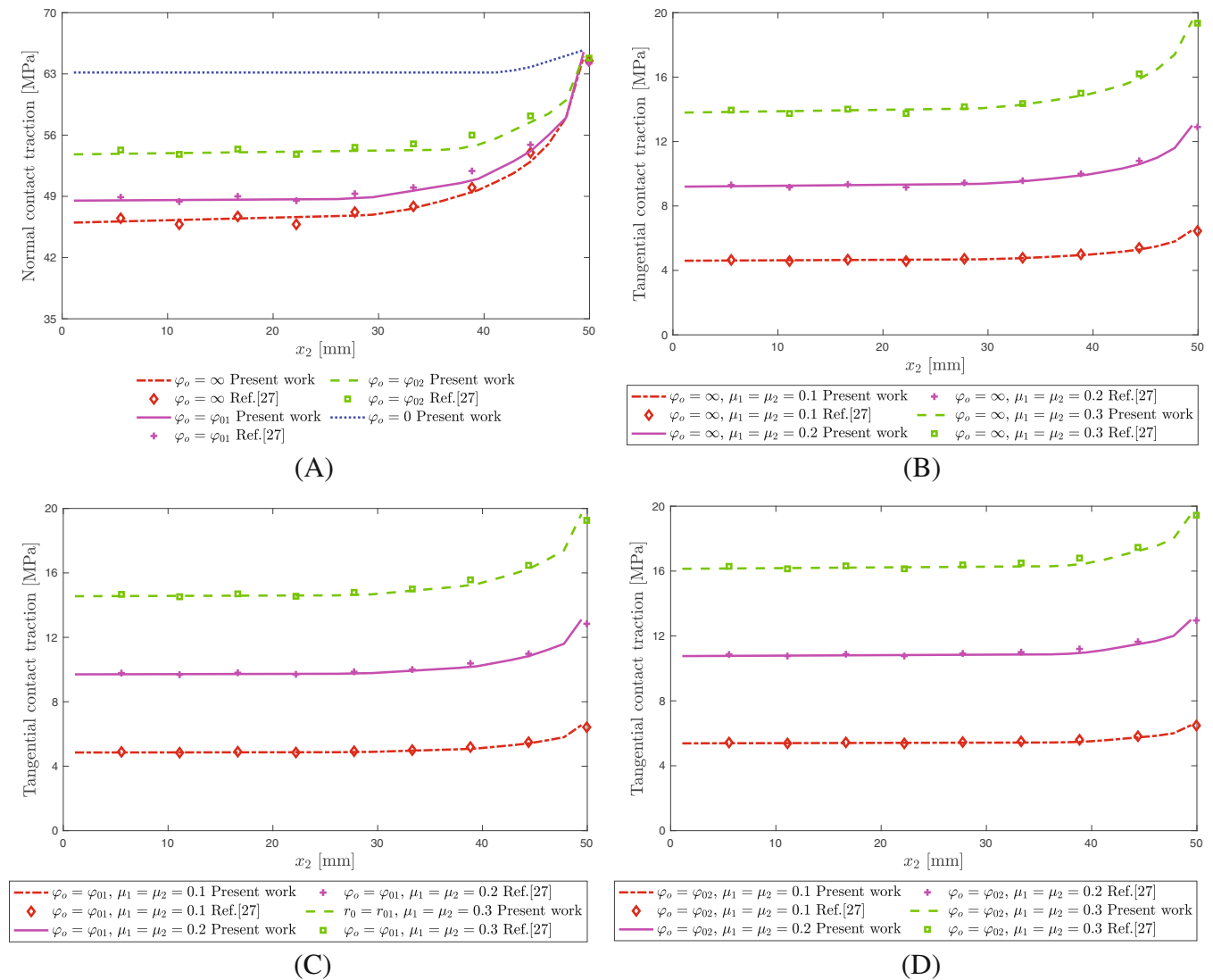


**FIGURE 6** Present formulation and 2D model<sup>27</sup> comparison for: (A) Normal contact tractions distribution. (B) Tangential contact tractions distribution for  $\varphi_0 = \infty$ . (C) Tangential contact tractions distribution for  $\varphi_0 = \varphi_{01}$ . (D) Tangential contact tractions distribution for  $\varphi_0 = \varphi_{02}$

Results reveal that the computed tangential traction values are  $\mu_1$  frictional coefficient values have no influence on the tangential traction distributions. Due to the dimensions of the solids, those are expected results, because these cases could be tackled as a  $x_2 - x_3$ -plane stress problems.

## 5.2 | Frictional heating effects

This example presents the influence of the frictional heating on the thermoelastic variables considering an orthotropic frictional law. The problem solved corresponds to the contact between a spherical punch of radius  $R = 100 \cdot 10^{-3}$  m over a rectangular solid with dimensions  $2L_1 \times 2L_1 \times L_2$  (see Figure 11), being  $L_1 = 50 \cdot 10^{-3}$  m and  $L_2 = 40 \cdot 10^{-3}$  m. The upper face of the spherical punch is set at a temperature of  $0^\circ\text{C}$ , whereas, at the rest of the faces, the heat flow is restricted  $q = 0$  W/mm<sup>2</sup>. However, on the block (or substrate), all its faces are set at a temperature of  $0^\circ\text{C}$ . The spherical punch is subjected to a normal indentation of  $g_{0_{x_3}} = 8 \cdot 10^{-5}$  m and to a different tangential sliding velocities ( $v_s$ ), which forms an angle  $\beta$  with axis  $x_1$  (see Figure 11). In this problem, a quasi-static thermoelastic contact problem can be considered since the formulation assumes that the axes are moving with the contact zone, which is moving with the punch. Therefore,

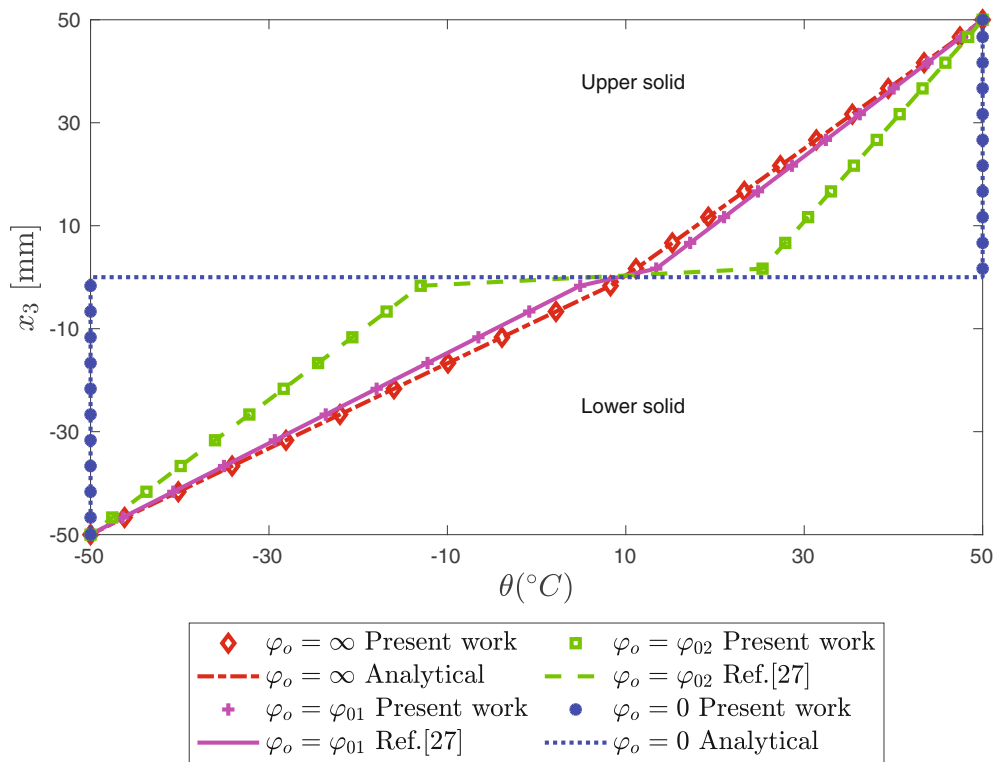


**FIGURE 7** Temperature variation comparison along the  $x_3$  axis between the proposed formulation and Reference 2D model<sup>27</sup>, as a function of the different thermal contact conductances studied

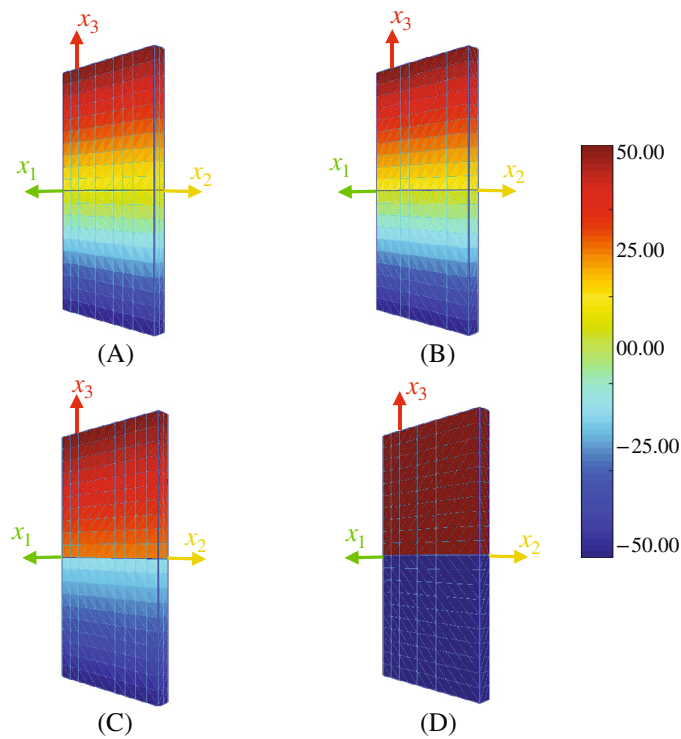


**FIGURE 8** Complete boundary temperature distribution of the 3D solids for the thermal contact conductance: (A)  $\varphi_0 = \infty$ . (B)  $\varphi_0 = \varphi_{01}$ . (C)  $\varphi_0 = \varphi_{02}$ . (D)  $\varphi_0 = 0$

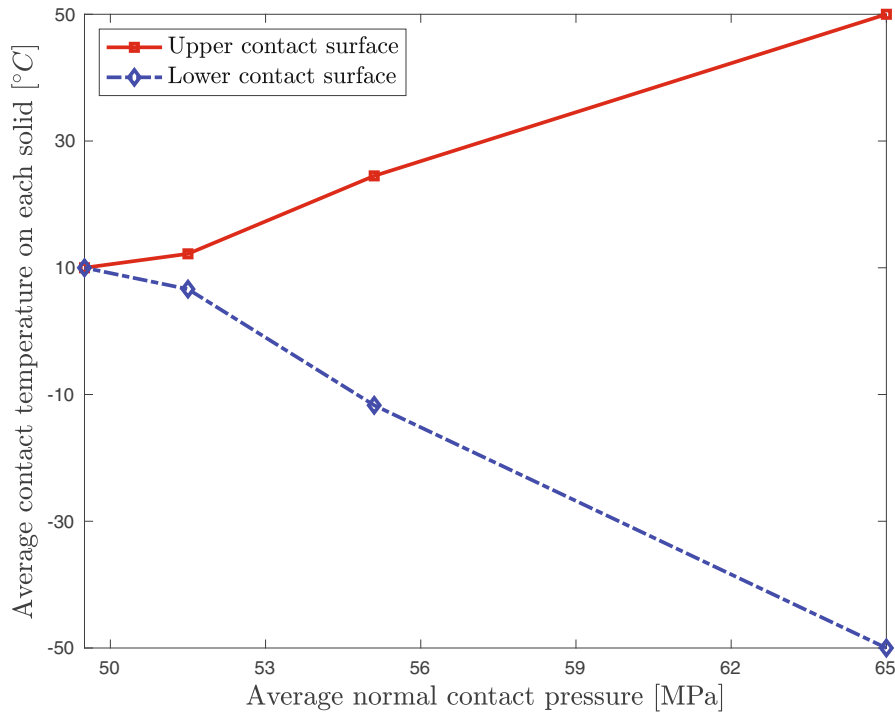


**FIGURE 9** Average contact temperature on each solid as a function of the normal contact pressure for each thermal contact conductance analyzed. The contact temperatures and contact normal pressures depend strongly on the thermal contact conductance

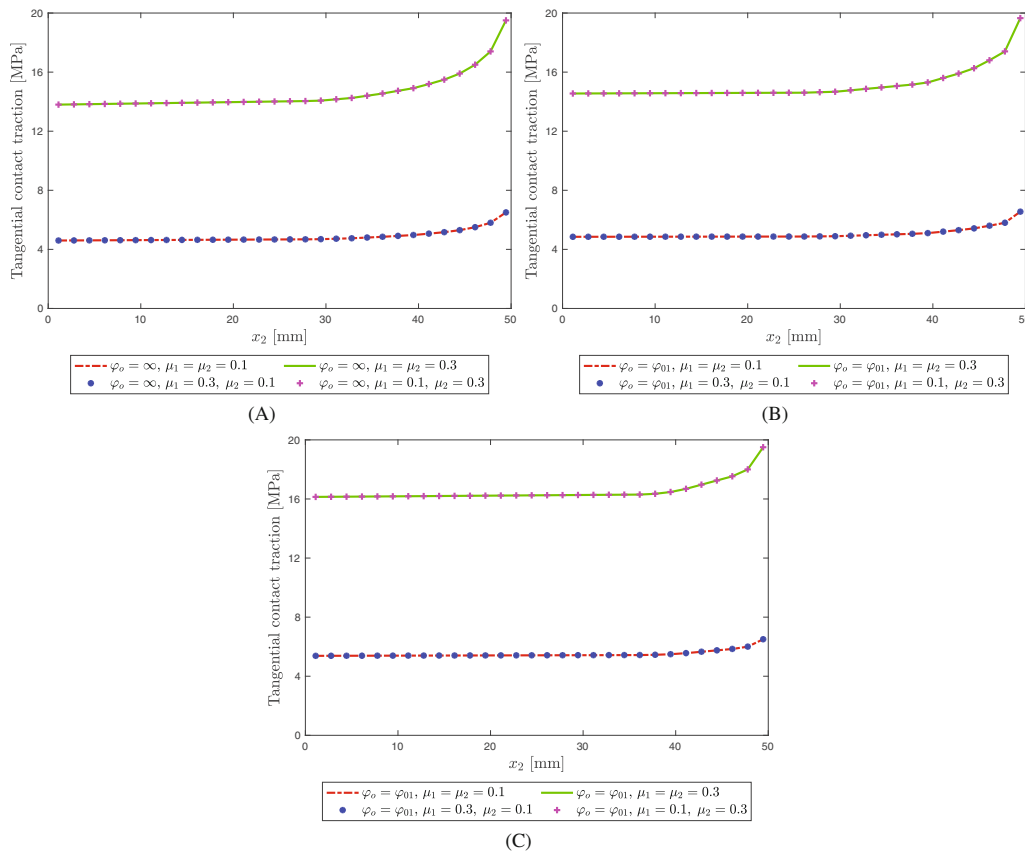


**FIGURE 10** Tangential traction comparison between isotropic ( $\mu_1 = \mu_2$ ) and orthotropic friction model ( $\mu_1 \neq \mu_2$ ) for: (A)  $\varphi_o = \infty$ . (B)  $\varphi_o = \varphi_{01}$ . (C)  $\varphi_o = \varphi_{02}$

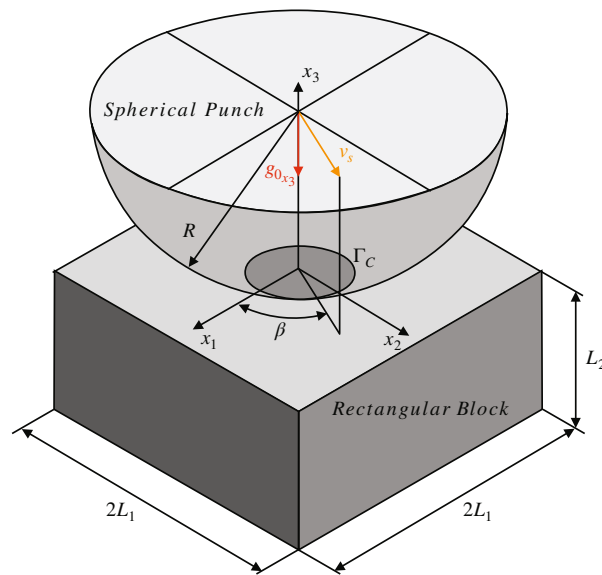


FIGURE 11 Geometry of a thermoelastic contact problem between a 3D spherical punch sliding over a rectangular solid

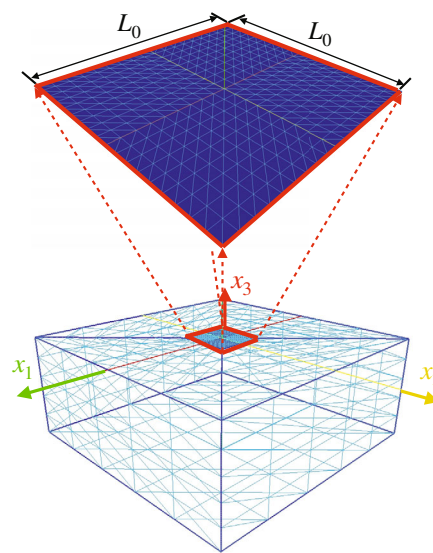


FIGURE 12 Boundary element discretization detail for the curved punch over a rectangular solid contact model

the tangential slip velocity on the contact zone is imposed on the potential contact zone nodes and its value is equal to the punch absolute velocity. Moreover, orthotropic frictional conditions ( $\mu_1 = 0.3$ ,  $\mu_2 = 0.1$ ) is considered. The potential contact ( $L_0 \times L_0$ , being  $L_0 = 10^{-3}$  m) zone has been discretized with a total of 648 elements. The boundary of the spherical punch and the rectangular solid has been discretized with a total of 450 elements respectively (Figure 12). In this example, it has been considered a zero thermal contact conductance ( $\varphi_0 = 0$ ) between both solids. The material parameters used are collected in Table 2.

Figure 13 shows the normalized normal contact traction distribution in the contact zone, where it can be seen that the results obtained match perfectly to those obtained with the Hertz solution.

Regarding the tangential tractions, Figure 14 presents the tangential slip vectors and the tangential traction modules for different directions of the imposed tangential sliding velocities. Only a quarter of the contact area has been represented and both the slip and tangential traction vectors have been plotted over the normal contact traction contour plot.

TABLE 2 Material parameters of the two solids

	Spherical punch	Rectangular block
E (GPa)	210	210
$\nu$	0.3	0.3
$\alpha$ ( $^{\circ}\text{C}^{-1}$ )	$2.0 \cdot 10^{-5}$	$1.0 \cdot 10^{-5}$
$k^l$ ( $\text{W}/^{\circ}\text{C mm}$ )	$80 \cdot 10^{-3}$	$10 \cdot 10^{-3}$
$\xi_{\mu}^l$	0.89	0.11

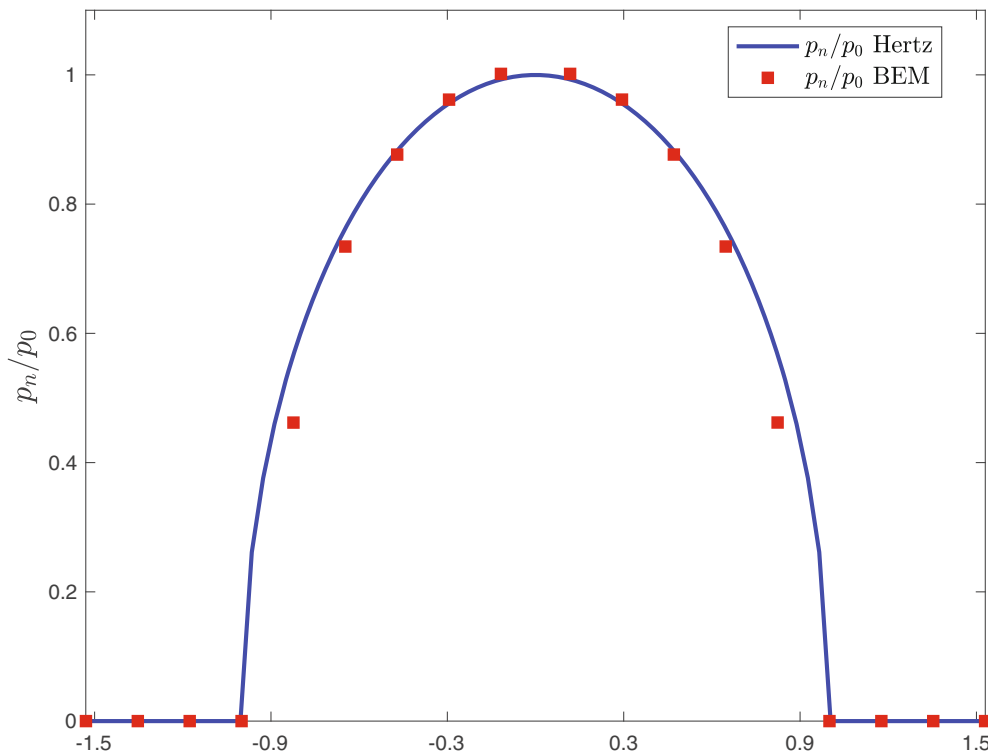


FIGURE 13 Normalized contact pressure distribution at the potential contact zone ( $\Gamma_c$ ). The contact radius is normalized by the Hertz contact radius  $a_0$

In Figure 14A–C, it can be seen how the slip and tangential tension vectors have opposite directions, satisfying the orthotropic frictional contact law ( $\mu_1 = \mu_2$ ). While, in Figure 14B, the tangential slip and tangential tension vectors satisfy the correlation  $\frac{p_{e_2}}{p_{e_1}} = \left(\frac{\mu_2}{\mu_1}\right)^2 \frac{\dot{g}_{e_2}}{\dot{g}_{e_1}}$  obtained from Reference 36, as it is shown in the Table 3.

On the other hand, Figure 15, shows the temperature distribution for the spherical punch, under the influence of different values of tangential velocity and sliding directions ( $\beta$ ). For both cases, the highest temperature is reached for the maximum tangential slip velocity and in the direction of the highest friction coefficient ( $\beta = 0^{\circ}$ ). In addition, Figure 16 shows the full distribution of temperatures in the potential contact zone of the spherical punch for  $v_s = 1000$  mm/s and  $\beta = 0^{\circ}, 45^{\circ},$  and  $90^{\circ}$  respectively.

In addition, Figure 17 shows the temperature comparison between considering the isotropic friction contact law and the orthotropic friction contact law. It is observed that when considering an isotropic friction law, the real values of temperatures are not collected, since we will obtain much higher values (Figure 17A) or much lower values (Figure 17C), than those we would obtain by considering an orthotropic friction law (Figure 17B), which is much closer to reality.

Finally, to show the convergence of the Uzawa method proposed in this work, Figure 18, shows the relative error and the number of iterations for the orthotropic friction law and different tangential slip velocity directions. For all cases, a



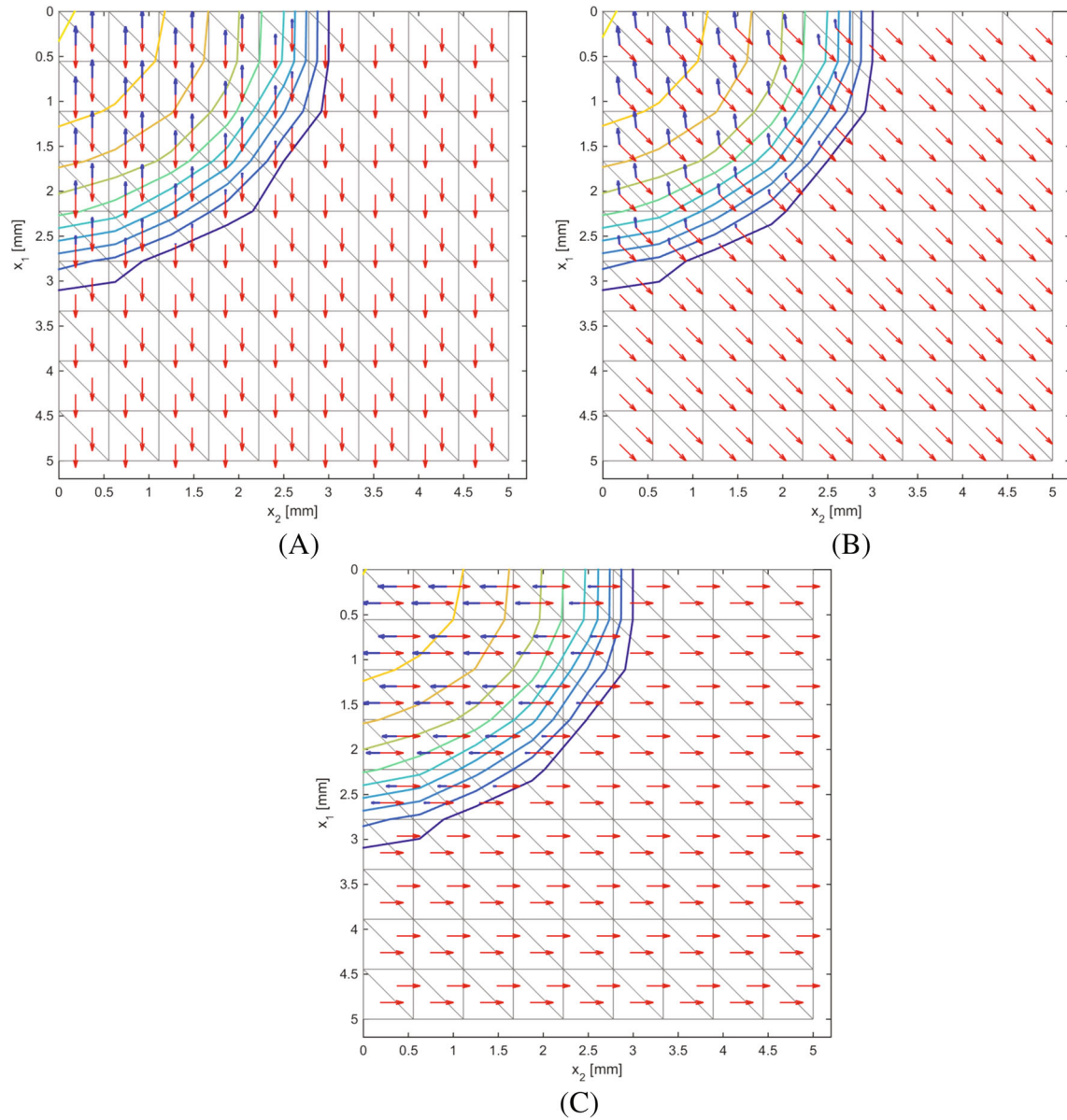


**FIGURE 14** Tangential slip vectors (red) and tangential traction vectors (blue) over normal contact pressure contour plot for: (A)  $\beta = 0^\circ$ . (B)  $\beta = 45^\circ$ . (C)  $\beta = 90^\circ$

**TABLE 3** Results on sliding contact points for:  $\mu_1 = 0.3$  and  $\mu_2 = 0.1$

$x_1$	$x_2$	$p_{e_1}$	$p_{e_2}$	$p_{e_2}/p_{e_1}$	$\dot{g}_{e_2}/\dot{g}_{e_1}$	$(\mu_2/\mu_1)^2 \dot{g}_{e_2}/\dot{g}_{e_1}$
0.19	0.37	-657.01	-73.00	0.11	1.00	0.11
0.19	0.93	-631.70	-70.19	0.11	1.00	0.11
0.19	1.48	-578.97	-64.33	0.11	1.00	0.11
0.19	2.04	-492.39	-54.71	0.11	1.00	0.11
0.19	2.59	-347.36	-38.60	0.11	1.00	0.11

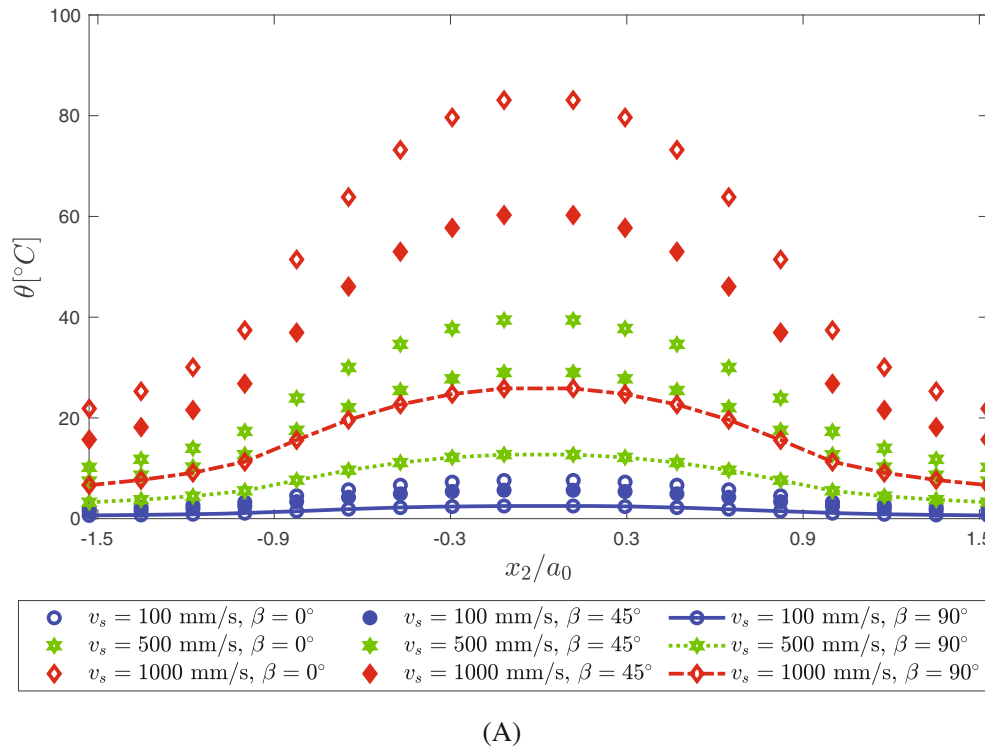


**FIGURE 15** Temperature distribution of the spherical punch for  $\varphi_o = 0$  and different slip directions ( $\beta$ ). The contact radius is normalized by the Hertz contact radius  $a_0$

similar convergence ratio is observed, with a higher number of iterations occurring in the direction where the friction coefficient is higher. More details of the algorithm used can be found in Reference 57, where a detailed study of the convergence of the Uzawa method is carried out.

### 5.3 | Effect of interstitial convective boundary conditions

Once it has been shown the effect that the heat generated by friction has on the thermomechanical variables. In this example, the influence of the introduction of a cutting fluid at the interface (TIM) and at interstitial contact zone as convective boundary conditions are studied. Geometry, mesh, boundary conditions, and materials properties are the same as previous example. The spherical punch is sliding at a tangential sliding velocity  $v_s = 1000$  mm/s and a different tangential sliding directions  $\beta$ . Orthotropic friction law is also considered ( $\mu_1 = 0.3$ ,  $\mu_2 = 0.1$ ). The contact conductance in the contact zone ( $\Gamma_c$ ) is calculated according to Reference 55 as it is presented in Section 3.3. Additionally, the thermal contact conductance ( $\varphi_o$ ) considers the existence of a TIM filling the microgaps by means of equations (24)–(22) and using parameters gathered in Table 4 and a thermal conductivity  $k_g = 0.7$  W/mK of the cutting fluid. However, in this example, this material will be also included surrounding the contact zone ( $\Gamma_c$ ), that is, in the non-contact area. This area has been designated as interstitial contact area ( $\Gamma_i^l$ ), so the potential contact area during the calculating process will be:  $\Gamma_{ic}^l = \Gamma_i^l \cup \Gamma_c$ , and convective conditions are considered  $\Gamma_i^l$ . The natural convection coefficient and forced convection coefficients are considered respectively  $h_f = 1000$  W/m<sup>2</sup>K and  $h_f = 10,000$  W/m<sup>2</sup>K.

Figure 19 shows how the introduction of a thermal conductance and fluid material at the interface (TIM) affect the maximum temperature at the potential contact area of the spherical punch. The temperature of the spherical punch decreases with the introduction of a thermal contact conductance ( $\varphi_o = \varphi_c$ ) and, moreover, it decreases further when the TIM is introduced ( $\varphi_o = \varphi_c + \varphi_g$ ), as it can be seen in Figure 19.

Figure 20 show how the thermoelastic contact response is affected by the addition or non-addition of the cutting fluid in the interface of the contact zone (TIM). Figure 20 presents the temperature distribution on the contact zone of

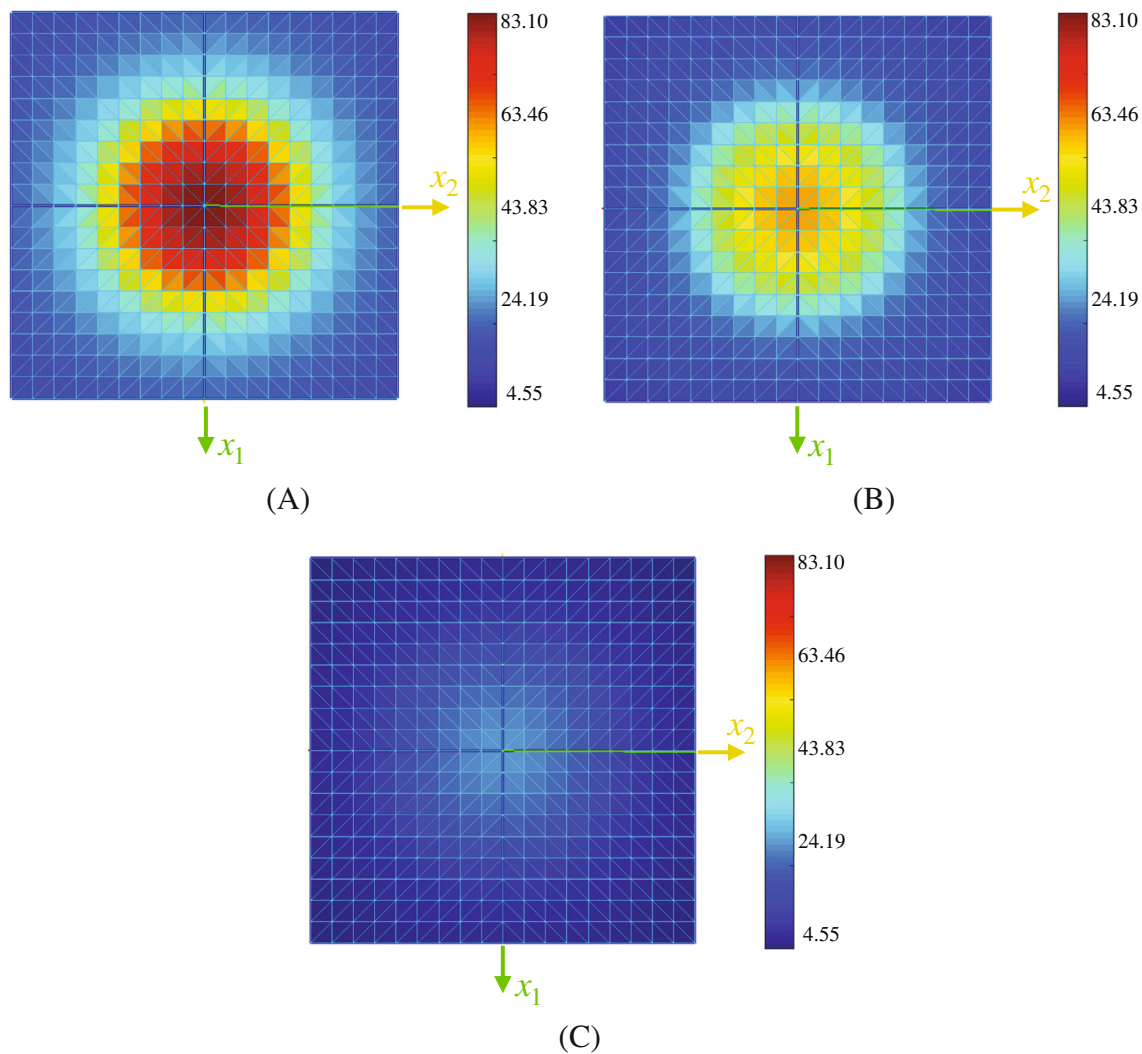
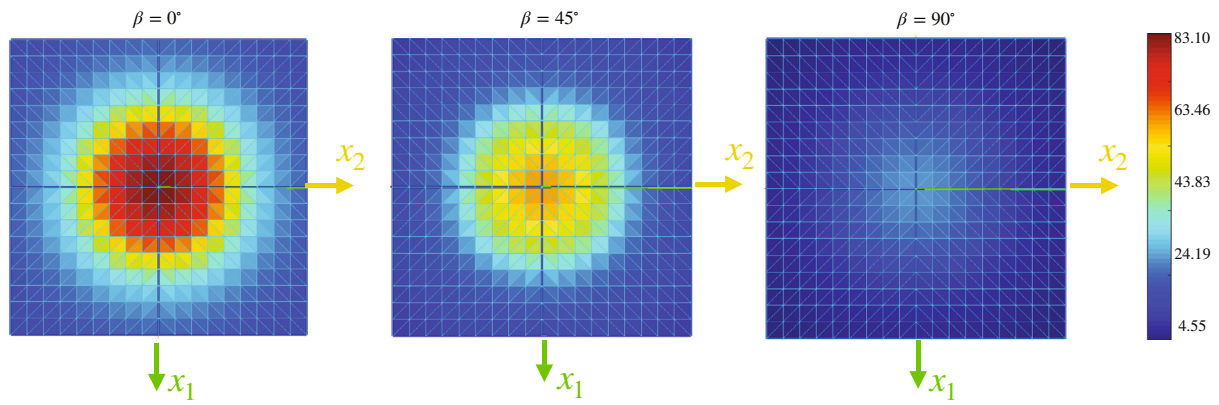


**FIGURE 16** Spherical punch temperature distribution for  $\phi_o = 0$ ,  $v_s = 1000$  mm/s and: (A)  $\beta = 0^\circ$ . (B)  $\beta = 45^\circ$ . (C)  $\beta = 90^\circ$

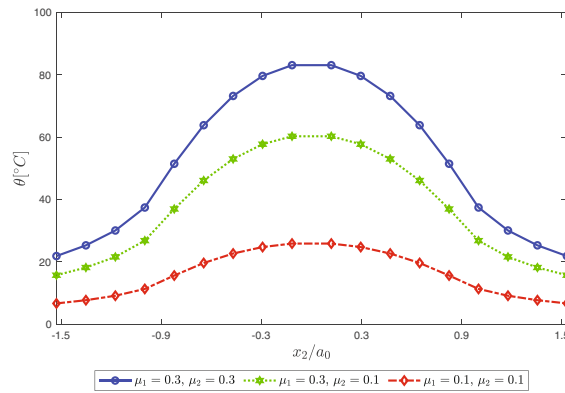
the spherical punch for different sliding directions ( $\beta$ ). It can be observed how the temperature of the spherical punch decreases with the sliding direction of the lower friction coefficients. Moreover, the introduction of the coolant produce a decrease in the temperature in the contact zone of the spherical punch.

In the same way, Figure 21 shows how the thermoelastic response of the potential contact zone is influenced by the presence of the cutting fluid and interstitial convective conditions for the sliding direction  $\beta = 0^\circ$ . Figure 21A shows the temperature distribution in the potential contact zone of the spherical punch for natural convection conditions and forced convection conditions for different temperature of the cutting fluid ( $\theta_f$ ). It can be observed how the introduction of the cutting fluid in the interface zone reduced the temperature of the spherical punch. Moreover, the temperature of the cutting fluid has also a great influence in the temperature distribution of the contact zone. As the temperature of the cutting fluid ( $\theta_f$ ) is reduced, the heat generated by friction is reduced, showing the effectiveness of the cutting fluid. However, natural convective conditions and cutting fluid at a temperature ( $\theta_f = 5^\circ$ ) in the interstitial zone have almost no influence on the temperature distribution.

In Figure 21B it is presented the heat fluxes distributions of both spherical punch and rectangular block for the same cases studied. The heat fluxes of the spherical punch are much higher than the rectangular block ones due to the higher conductivity ( $k^l$ ) of the spherical punch in both final contact zone and interstitial zone. In the same way as the temperature distribution, the heat fluxes distribution for both spherical punch and rectangular block is the same for natural convection conditions at the interstitial zone. Moreover, the heat fluxes of the rectangular block are strongly influenced by the temperature of the fluid in the interphase. It is observed that the heat flux



(A)



(B)

**FIGURE 17** (A) Spherical punch temperature distribution comparison for  $\dot{g}_t=1000$  mm/s and  $\beta = 45^\circ$  for:  $\mu_1 = 0.3, \mu_2 = 0.3, \mu_1 = 0.3, \mu_2 = 0.1$ , and  $\mu_1 = 0.1, \mu_2 = 0.1$ . (B) Temperature comparison between isotropic and orthotropic friction law. The contact radius is normalized by the Hertz contact radius  $a_0$

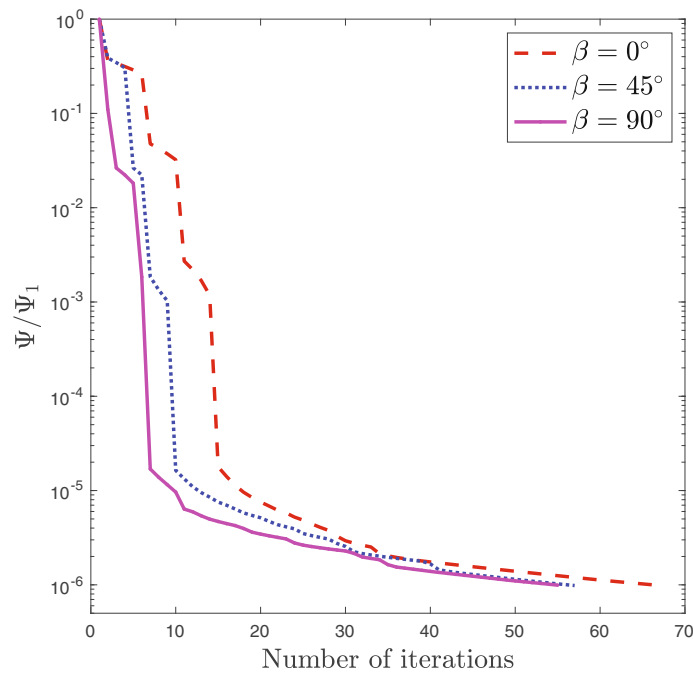


**FIGURE 18** Error evolution as a function of the tangential slip direction ( $\beta$ )

TABLE 4 Parameters of the thermal conductance model used

	$m^A$	$m^B$	$H^A$	$H^B$	$\sigma^A$	$\sigma^B$
$\varphi_o$	$5.0 \cdot 10^{-3}$	$5.0 \cdot 10^{-3}$	2460	2460	$5.0 \cdot 10^{-3}$	$5.0 \cdot 10^{-3}$

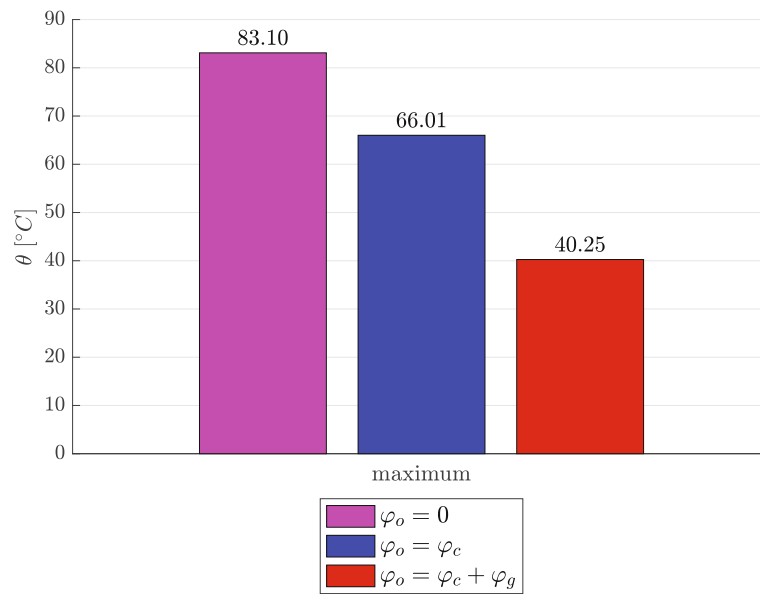


FIGURE 19 Maximum temperature ( $\theta_{max}$ ) at the potential contact zone of the spherical punch for  $\dot{g}_t=1000$  mm/s and  $\beta = 0^\circ$ :  $\varphi_o = 0$ ,  $\varphi_o = \varphi_c$ ,  $\varphi_o = \varphi_c + \varphi_g$

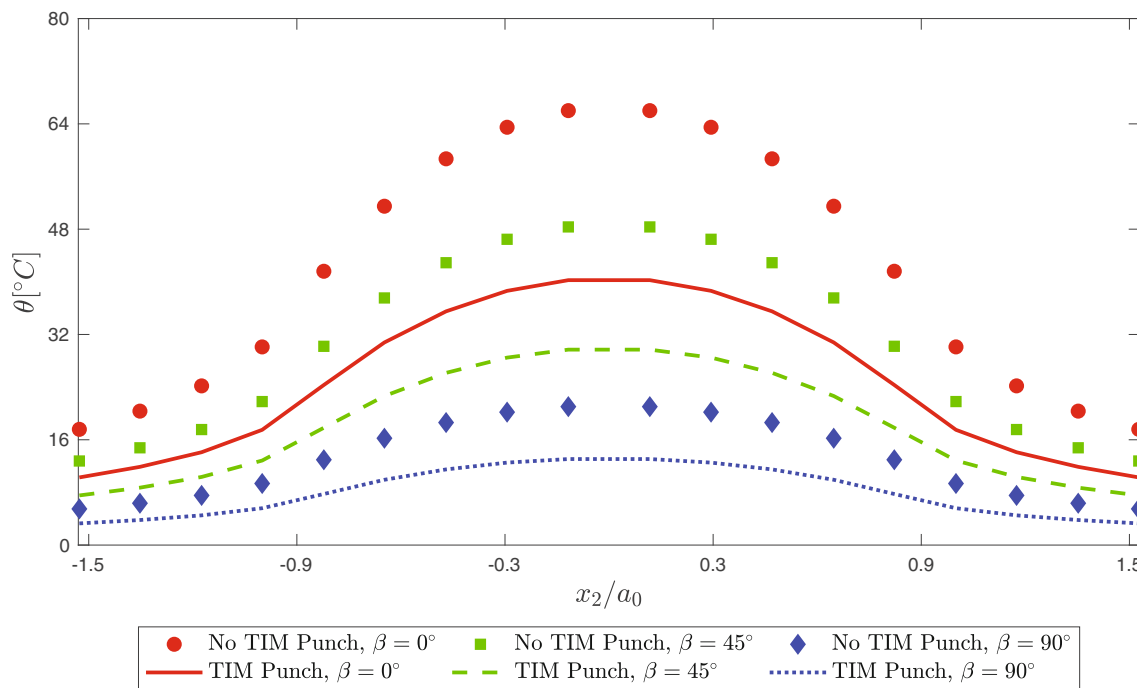
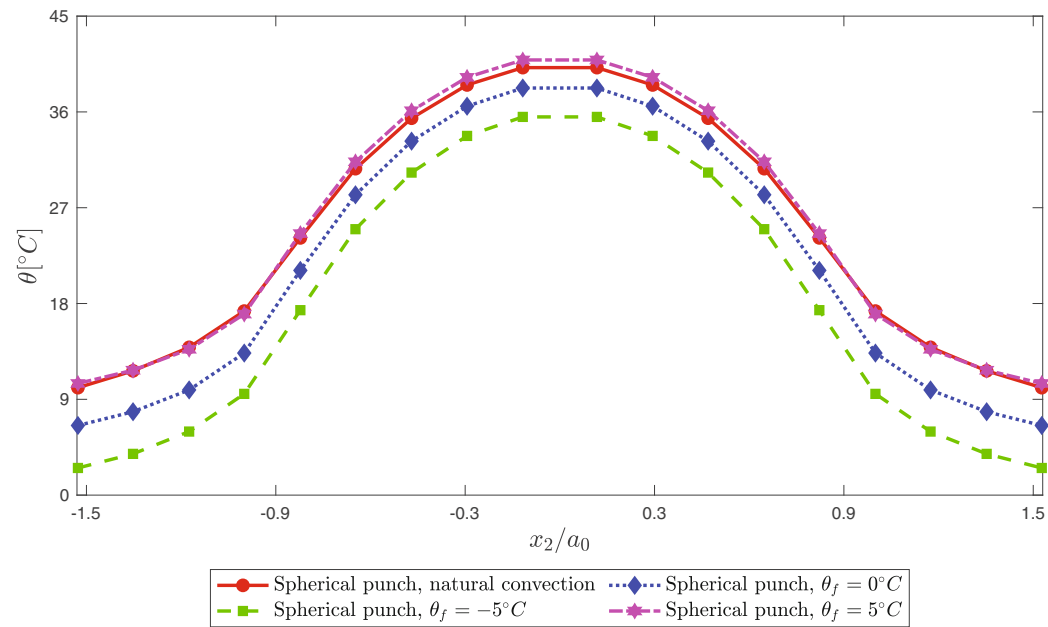
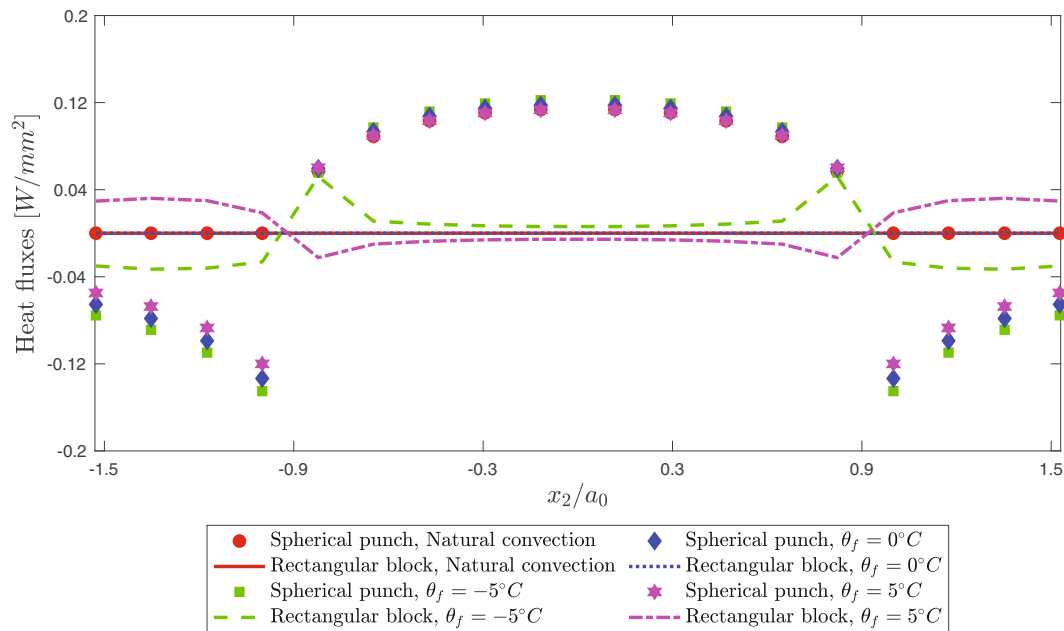


FIGURE 20 Temperature distribution comparison for no TIM addition conditions and for TIM addition conditions at the spherical punch. The contact radius is normalized by the Hertz contact radius  $a_0$



(A)



(B)

**FIGURE 21** Thermomechanical contact response comparison for forced convection with  $\theta_f = -5^\circ\text{C}$ ,  $\theta_f = 0^\circ\text{C}$ , and  $\theta_f = 5^\circ\text{C}$  and for natural convection in the: (A) Temperature distribution of the spherical punch. (B) Heat fluxes distribution for both spherical punch and rectangular block. The contact radius is normalized by the Hertz contact radius  $a_0$

is zero when the temperature of the fluid and the rectangular block are equal ( $\theta_f = \theta^B = 0^\circ$ ). However, when the temperature of the cutting fluid ( $\theta_f$ ) is smaller than the rectangular block temperature, the heat flux values increases in the contact zone. The opposite occurs in the contact zone when the temperature of the cutting fluid ( $\theta_f$ ) is higher than the temperature of the rectangular block. Moreover, in both cases, the heat flow direction at the interstitial zone reverses.

Finally, the complete temperature distribution of the potential contact zone of the spherical punch for the cases of studied is presented in Figure 22. The great influence of the temperature of the cutting fluid ( $\theta_f$ ) in the temperature distribution is shown.



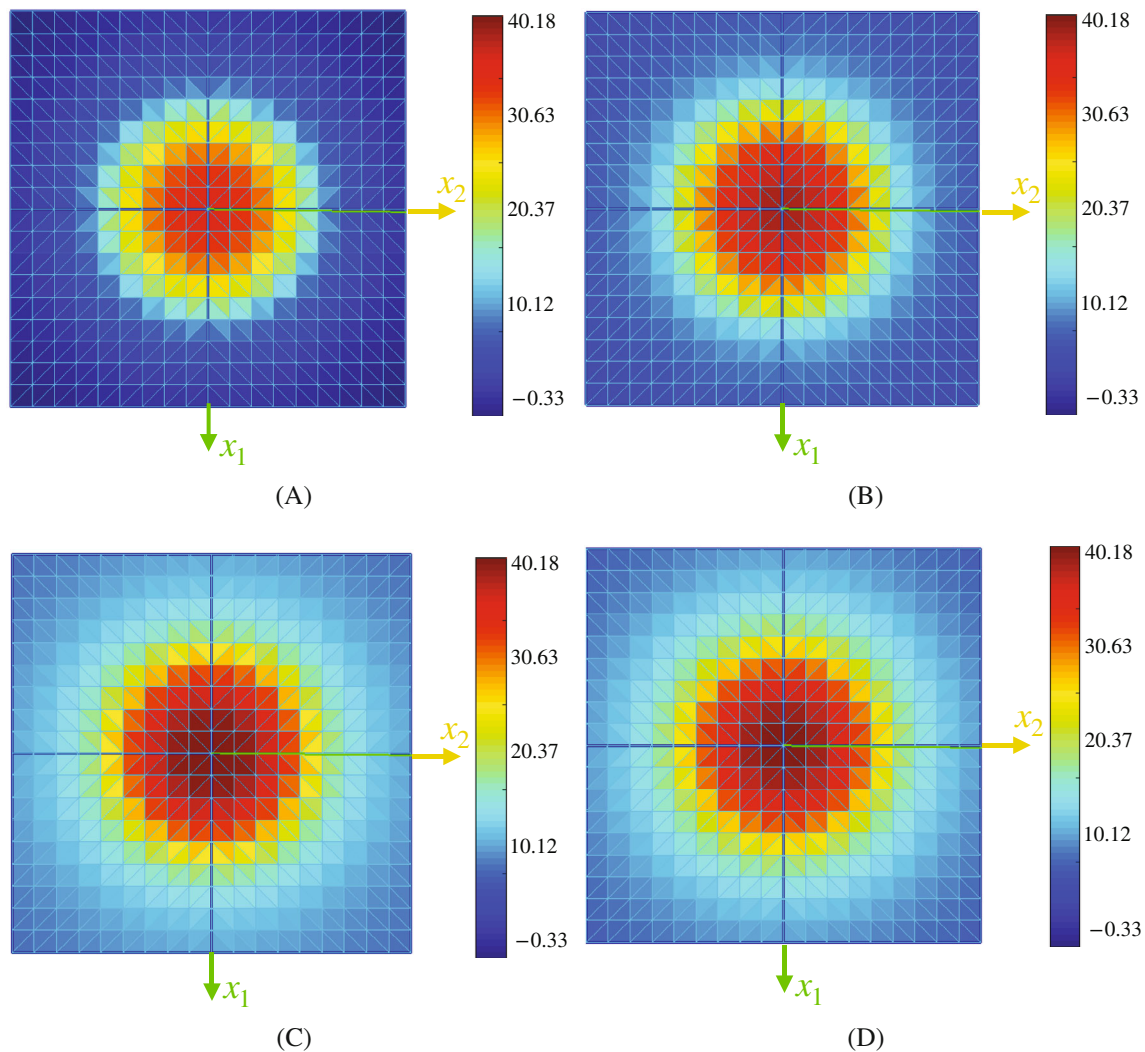


**FIGURE 22** Spherical punch temperature distribution for  $\beta = 0^\circ$  for: (A) Forced convection with  $\theta_f = -5^\circ\text{C}$ . (B) Forced convection with  $\theta_f = 0^\circ\text{C}$ . (C) Forced convection with  $\theta_f = 5^\circ\text{C}$ . (D) Natural convection

## 5.4 | Brake disc-pad contact

Finally, in this example, a brake disc-pad system model is studied. During braking, the pad can rotate slightly, which may affect its functionality. For this reason, the temperature and tractions values in the contact zone between the pad and the disc are analyzed. The disc is sliding at a tangential sliding velocity  $v_s = 10,000$  mm/s and the pad rotation during operation is simulated by different sliding directions  $\beta$  with axis  $x_1$ . The upper face of the pad is set at a temperature of  $0^\circ\text{C}$  and on the rest of the faces, the heat flow is restricted,  $q = 0$  W/mm<sup>2</sup>. The temperature of the disc has been set constant and equal to that produced by friction after passing very fast and many times through the brake pad. It is also considered that the pad is subjected to a normal displacement of  $g_{0,x_3} = 5 \cdot 10^{-5}$  m during braking. Moreover, orthotropic friction law is also considered ( $\mu_1 = 0.3$ ,  $\mu_2 = 0.1$ ). The geometry of the model and the complete system modeled with boundary elements is shown in Figure 23 and in Figure 24 respectively. The contact zone has been meshed with a total of 704 elements. The boundary of the pad and the disc has been discretized with 192 and 188 elements respectively. Material properties used are obtained from References 58,59 and are gathered in Table 5. In this example, it has been considered an infinity thermal contact conductance ( $\varphi_0 = \infty$ ) between both solids.

In relation with the temperature results, Figure 25 shows the maximum temperature of the pad and the disc is shown as a function of the thermal contact conductances ( $\varphi_0$ ) and for non rotation of the pad ( $\beta = 0^\circ$ ).

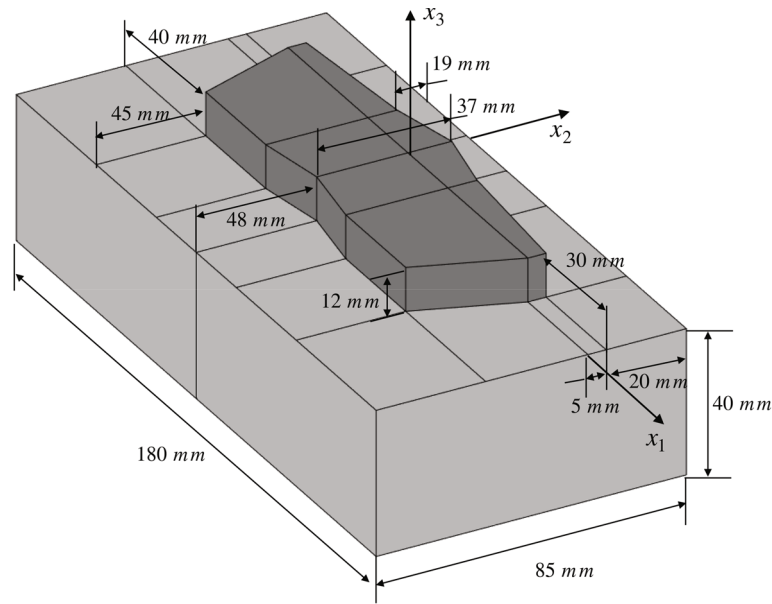


FIGURE 23 Geometry of the break disc-pad contact model analyzed

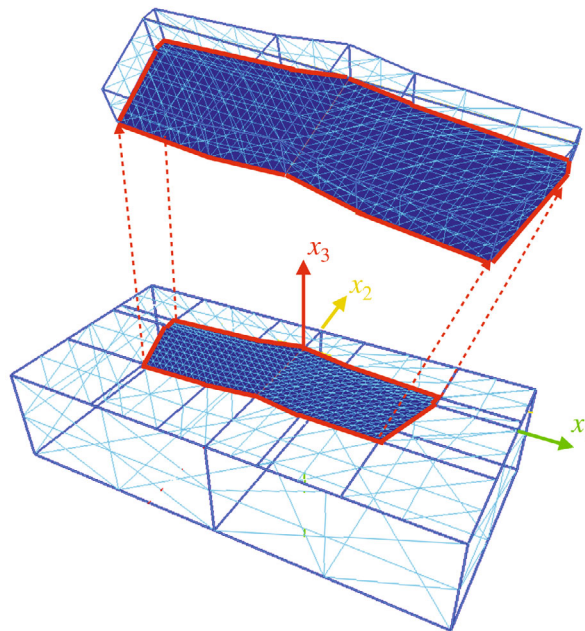


FIGURE 24 Boundary element discretization detail for the break disc-pad contact model

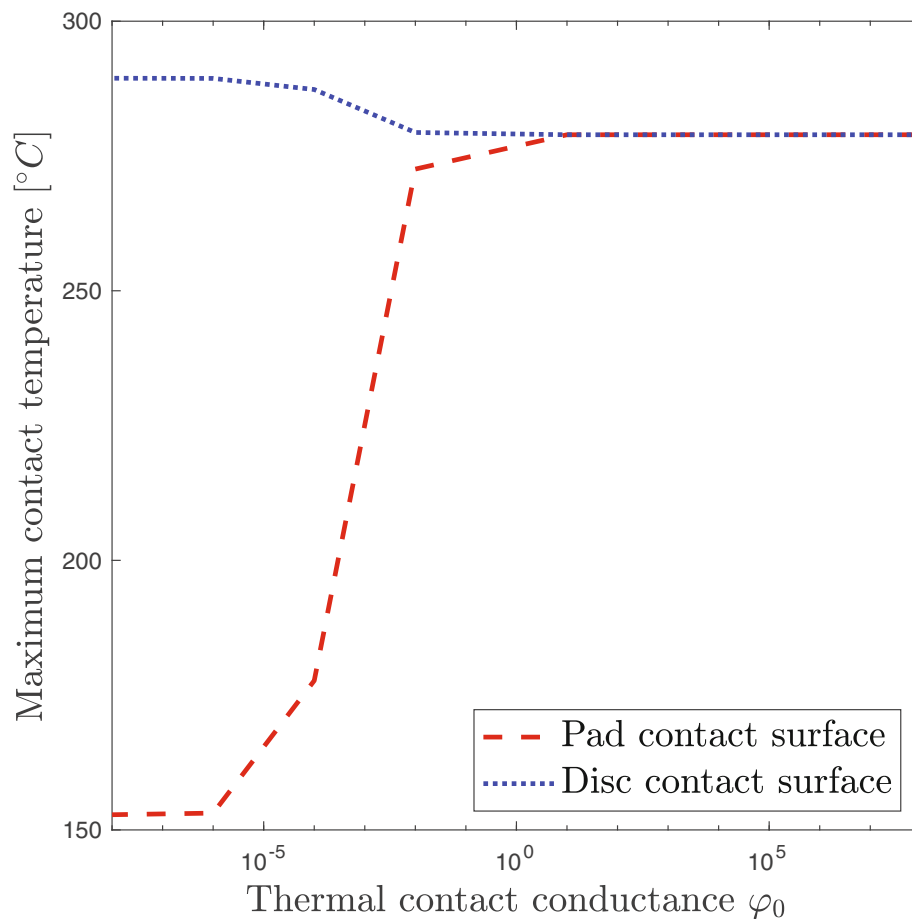
The temperatures of the disc depend greatly on the thermal contact conductances being highest for values of zero thermal contact conductance. The temperature of the disc decreases as the value of the thermal contact conductance increases and converges toward the maximum temperature of the pad. The behavior of the maximum temperature of the pad is the opposite. The maximum temperature increases with increasing the thermal contact conductance.

On the one hand, Figure 26 shows the complete temperature distribution for an infinity thermal contact conductance ( $\varphi_0 = \infty$ ) and a rotation of the pad during braking of  $\beta = 0^\circ$ ,  $5^\circ$ ,  $10^\circ$ , and  $15^\circ$  respectively. It is observed that the temperature of the disc-pad system decreases as the rotation ( $\beta$ ) of the pad increases. This effect is produced by the loss of influence



TABLE 5 Material parameters of the dis-pad contact model

	Pad	Disc
E (GPa)	1	138
$\nu$	0.3	0.3
$\alpha$ ( $^{\circ}\text{C}^{-1}$ )	$1.0 \cdot 10^{-5}$	$1.85 \cdot 10^{-5}$
$k^l$ ( $\text{W}/^{\circ}\text{C mm}$ )	$5 \cdot 10^{-3}$	$57 \cdot 10^{-3}$
$\xi_{\mu}^l$	0.08	0.92

FIGURE 25 Maximum temperature in the pad and the disc as functions of the thermal contact conductance  $\varphi_0$ 

of the friction coefficient in the direction  $x_1$  and the consequent decrease of the tangential traction values responsible of the braking, as shown in Figure 27.

On the other hand, Figure 27 shows the complete tangential traction distribution of the complete contact zone. Analogous to the temperature values, the value of the tangential traction decreases as the brake pad rotation ( $\beta$ ) increases, so the braking effectiveness is reduced.

## 6 | SUMMARY AND CONCLUSIONS

This work presents a boundary element formulation to study the thermomechanical surface interaction between two three-dimensional solids under advance thermoelastic contact conditions, that is, orthotropic frictional contact conditions and non-linear interface thermoelastic contact conditions (including the implementation of interstitial convective boundary conditions). They result in a multifield conditions set which are imposed by means of projection

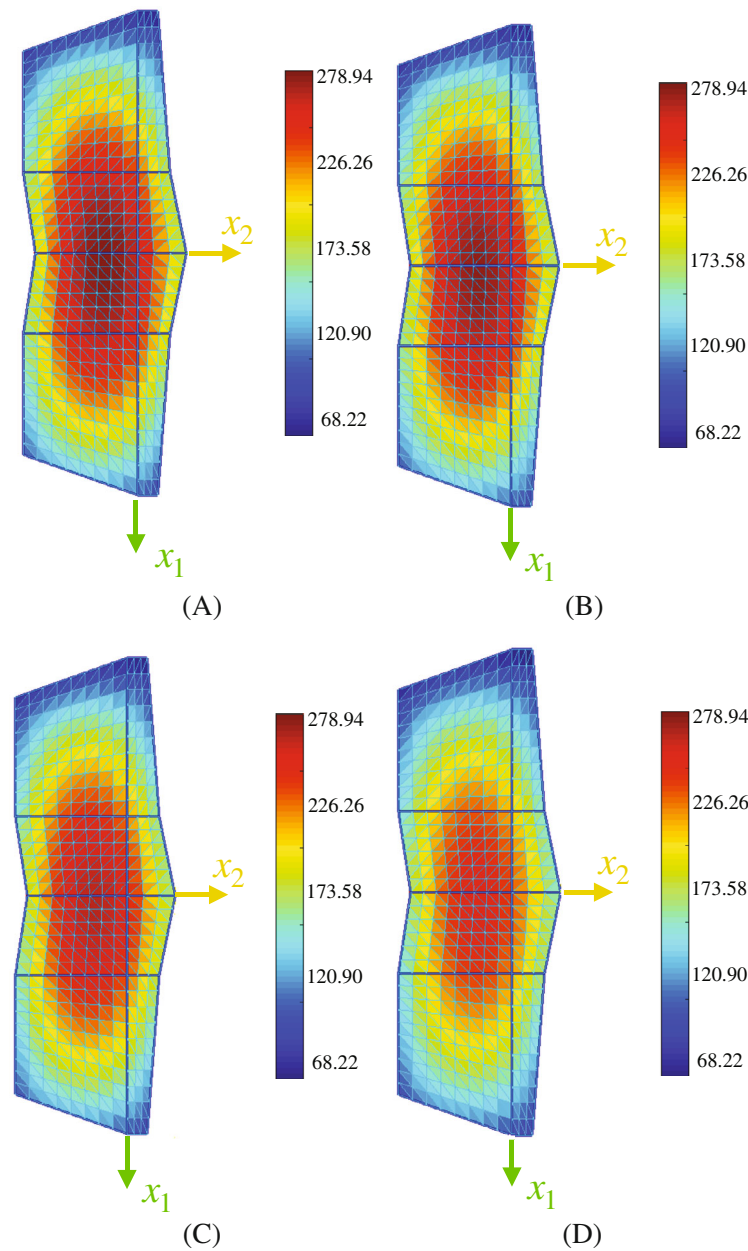


FIGURE 26 Temperature distribution for the pad for  $\varphi_0 = \infty$  for: (A)  $\beta = 0^\circ$ . (B)  $\beta = 5^\circ$ . (C)  $\beta = 10^\circ$ . (D)  $\beta = 15^\circ$

functions and an Augmented Lagrangian formulation, resulting in a very compact and robust formulation for quasi-static thermomechanical contact problems.

The formulation and the proposed solution scheme have been validated and applied to study the combined effects of considering an orthotropic friction law, interstitial convective conditions and the presence of a TIM on the thermomechanical contact variables. Moreover, the influence of the orthotropic friction law and the frictional heating is also studied in a brake disc-pad contact system. After these studies, the main conclusions and findings of this works are:

- The thermal contact conductance has a great influence in the thermoelastic contact variables. Small thermal conductance values leads to high temperature jumps on the surfaces in contact.
- Orthotropic frictional heating also presents significant influence in the thermomechanical variables. The temperature and the heat fluxes of the contact surfaces are not also greatly affected by the sliding velocity module ( $v_s$ ), but also the sliding direction ( $\beta$ ).

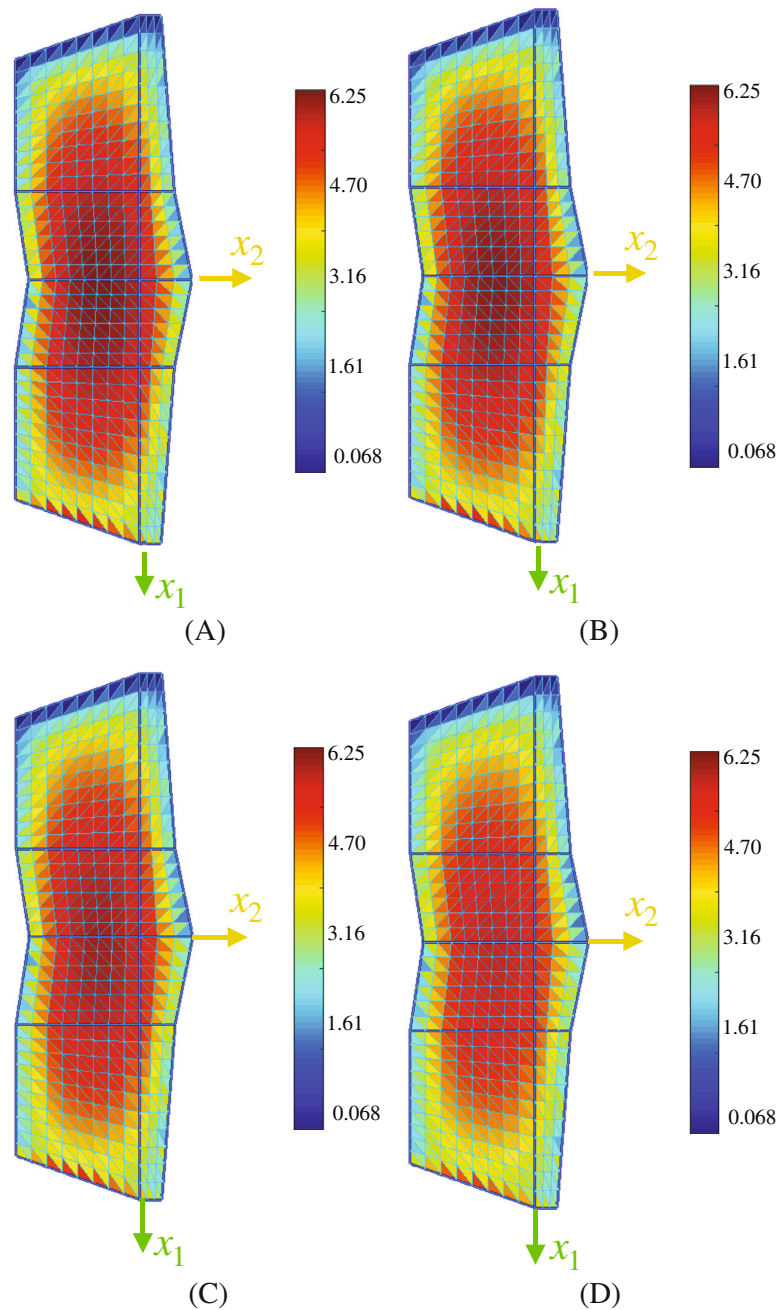


FIGURE 27 Tangential traction distribution for the pad for  $\varphi_o = \infty$  for: (A)  $\beta = 0^\circ$ . (B)  $\beta = 5^\circ$ . (C)  $\beta = 10^\circ$ . (D)  $\beta = 15^\circ$

- The assumption of an isotropic friction law under orthotropic friction conditions can over- or under-estimate the frictional heating effect, resulting temperature distributions in solids. Consequently, realistic tribological friction laws (e.g., orthotropic law) should be considered in these studies.
- The influence of convective interstitial boundary conditions on the frictional heating effects should be also incorporated to the analysis. The results reveal that these effects can be highly reduced when low temperatures of the interstitial fluid ( $\theta_f$ ) and forced convection conditions are considered.

Finally, it is important to mention that the proposed formulation has a lot of potential applications in modern engineering technologies where the frictional effects in the contact problems is relevant such as in a brake disc-pad contact system. Moreover, the formulation herein proposed may be extended to consider the influence of wear in thermomechanical contact problems.


## ACKNOWLEDGMENT

This research work has been supported by the Universidad de León. L. Rodríguez-Tembleque was also supported by the VI Plan Propio de Investigación de la Universidad de Sevilla (Ayuda del VI-PPI I.3A).

## DATA AVAILABILITY STATEMENT

The authors confirm that the data supporting the findings of this study are available within the article. Furthermore, if any additional data be required, they are available upon reasonable request to the corresponding editor [I. Ubero-Martínez].

## ORCID

Iván Ubero-Martínez  <https://orcid.org/0000-0003-4236-9298>

## REFERENCES

1. Curnier A. A theory of friction. *Int J Solids Struct.* 1984;7:637-647.
2. Michalowski R, Mróz Z. Associated and non-associated sliding rules in contact friction problems. *Int J Solids Struct.* 1994;31:1113-1131.
3. Zmitrowicz A. A mathematical descriptions of anisotropic friction. *Int J Solids Struct.* 1989;25:837-862.
4. Zmitrowicz A. An equation of anisotropic friction with sliding path curvature effects. *Int J Solids Struct.* 1999;36:2825-2848.
5. Zmitrowicz A. Models of kinematics dependent anisotropic and heterogeneous friction. *Int J Solids Struct.* 2006;43:4407-4451.
6. Johnson K. *Contact Mechanics.* Cambridge University Press; 1985.
7. Hills D, Nowell D, Sackfield A. *A Mechanics of Elastic Contact.* Butterworth-Heinemann; 1993.
8. Buczkowski R, Kleiber M. Elasto-plastic interface model for 3D-frictional orthotropic contact problems. *Int J Numer Methods Eng.* 1997;40:599-619.
9. Feng ZQ, Hjiat M, Saxcé GD, Mróz Z. Effect of frictional anisotropy on the quasistatic motion of a deformable solid sliding on a planar surface. *Comput Mech.* 2006;37:349-361.
10. Joli P, Feng ZQ. Uzawa and Newton algorithms to solve frictional contact problems within the bi-potential framework. *Int J Numer Methods Eng.* 2008;73:317-330.
11. Buczkowski R, Kleiber M. Statical models of rough surfaces for finite numerical 3D contact analysis. *Arch Comput Methods Eng.* 2009;16:399-424.
12. Zavarise G, Wriggers P, Stein E, Schrefler BA. A numerical model for thermomechanical contact based on microscopic interface laws. *Mech Res Commun.* 1992;19(3):173-182.
13. Zavarise G, Wriggers P, Stein E, Schrefler BA. Real contact mechanisms and finite element formulation. A coupled thermomechanical approach. *Int J Numer Methods Eng.* 1992;35:767-785.
14. Wriggers P, Zavarise G. Thermomechanical contact - A rigorous but simple numerical approach. *Comput Struct.* 1993;46(1):47-53.
15. Johansson L, Klarbring A. Thermoelastic frictional contact problems: modelling, finite element approximation and numerical realization. *Comput Methods Appl Mech Eng.* 1993;105:181-210.
16. Strömberg N. Finite element treatment of two-dimensional thermoelastic wear problems. *Comput Methods Appl Mech Eng.* 1999;177:441-455.
17. Ireman P, Klarbring A, Strömberg N. Finite element algorithms for thermoelastic wear problems. *Eur J Mech A/Solids.* 2002;21:423-440.
18. Lundvall O, Strömberg N, Klarbring A. A flexible multi-body approach for frictional contact in spurs gears. *J Sound Vib.* 2004;278:479-499.
19. Strömberg N. An Eulerian approach for simulating frictional heating in disc-pad systems. *Eur J Mech A/Solids.* 2011;30:673-683.
20. Strömberg N. An Eulerian-based thermo-flexible multi-body approach for simulating rig testing of disc brakes. computational and experimental methods in structures. In: Rodríguez-Tembleque Luis, Aliabadi MHF, eds. *Advances in Computational Coupling and Contact Mechanics.* Word Scientific; 2018:179-195.
21. Pantuso D, Bathe KJ, Bouzinov PA. A finite element procedure for the analysis of thermomechanical solids in contact. *Comput Struct.* 2000;75:551-573.
22. Hüeber S, Wohlmuth BI. Thermo-mechanical contact problems on non-matching meshes. *Comput Methods Appl Mech Eng.* 2009;198:1338-1350.
23. Seitz A, Wall WA, Popp A. Nitsche's method for finite deformation thermomechanical contact problems. *Comput Mech.* 2019;63:1091-1110.
24. Aliabadi FMH. *The Boundary Element Method: Applications in Solids and Structures.* Vol 2. Wiley; 2002.
25. Kikuo Kishimoto K, Inoue H, Shibuya T. Boundary element analysis of thermoelastic contact problems. *Eng Anal Bound Elem.* 1995;15:329-337.
26. Alonso P, Garrido GJ. BEM applied to 2D thermoelastic contact problems including conduction and forced convection in interstitial zones. *Eng Anal Bound Elem.* 1995;15(3):249-259. doi:10.1016/0955-7997(95)00029-N
27. Giannopoulos GI, Anifantis NK. A BEM analysis for thermomechanical closure of interfacial cracks incorporating friction and thermal resistance. *Comput Methods Appl Mech Eng.* 2007;196(4-6):1018-1029. doi:10.1016/j.cma.2006.08.013
28. Vallepuja Espinosa J, Foces Mediavilla A. Boundary element method applied to three dimensional thermoelastic contact. *Eng Anal Bound Elem.* 2012;36(6):928-933. doi:10.1016/j.enganabound.2011.12.010
29. Hematiyan M, Khosravifard A, Shiah Y. A novel inverse method for identification of 3D thermal conductivity coefficients of anisotropic media by the boundary element analysis. *Int J Heat Mass Transf.* 2015;89:685-693.
30. Dargush GF, Soom A. Contact modeling in boundary element analysis including the simulation of thermomechanical wear. *Tribol Int.* 2016;100:360-370. doi:10.1016/j.triboint.2016.04.001

31. Ubero-Martinez I, Vallepuga-Espinosa J, Rodríguez-Tembleque L, Cifuentes-Rodríguez J. The effect of conduction and convective conditions at interstitial regions on 3D thermoelastic contact problems. *Eng Anal Bound Elem*. 2019;107:243-256.
32. Vallepuga-Espinosa J, Ubero-Martinez I, Cifuentes-Rodríguez J, Rodríguez-Tembleque L. Thermoelastic influence of convective and conduction interstitial conditions on the size of the contact zone in three-dimensional receding thermoelastic contact problem. *Acta Mech*. 2020;231(7):3065-3084.
33. Vallepuga-Espinosa J, Ubero-Martinez I, Rodríguez-Tembleque L, Cifuentes-Rodríguez J. A boundary element procedure to analyze the thermomechanical contact problem in 3D microelectronic packaging. *Eng Anal Bound Elem*. 2020;115:28-39.
34. Ubero-Martinez I, Rodríguez-Tembleque L, Cifuentes-Rodríguez J, Vallepuga-Espinosa J. Non-linear interface thermal conditions in three-dimensional thermoelastic contact problems. *Comput Struct*. 2020;241(106354). doi:10.1016/j.compstruc.2020.106354
35. Shiah Y, Chang RY, Hematiyan M. Three-dimensional analysis of heat conduction in anisotropic composites with thin adhesive/interstitial media by the boundary element method. *Eng Anal Bound Elem*. 2021;123:36-47.
36. Rodríguez-Tembleque L, Abascal R. Fast FE-BEM algorithms for orthotropic frictional contact. *Int J Numer Methods Eng*. 2013;94(7):687-707.
37. Rodríguez-Tembleque L, Buroni FC, Abascal R, Sáez A. Analysis of FRP composites under frictional contact conditions. *Int J Solids Struct*. 2013;50:3947-3959.
38. Rodríguez-Tembleque L, García-Macías E, Sáez A. CNT-polymer nanocomposites under frictional contact conditions. *Compos B*. 2018;154:114-127.
39. Rodríguez-Tembleque L, Buroni FC, Sáez A. 3D BEM for orthotropic frictional contact of piezoelectric bodies. *Comput Mech*. 2015;56:491-502.
40. Rodríguez-Tembleque L, Sáez A, Aliabadi M. Indentation response of piezoelectric films under frictional contact. *Int J Eng Sci*. 2016;107:36-53.
41. Rodríguez-Tembleque L, Buroni FC, Sáez A, Aliabadi MH. 3D coupled multifield magneto-electro-elastic contact modelling. *Int J Mech Sci*. 2016;114:35-51.
42. Rodríguez-Tembleque L, Aliabadi MH. Numerical simulation of fretting wear in fiber-reinforced composite materials. *Eng Fract Mech*. 2016;168:13-27.
43. Giannopoulos GI, Anifantis NK. Interfacial steady-state and transient thermal fracture of dissimilar media using the boundary element contact analysis. *Int J Numer Methods Eng*. 2005;62:1399-1420.
44. Keppas LK, Giannopoulos GI, Anifantis NK. Transient coupled thermoelastic contact problems incorporating thermal resistance: a BEM approach. *Comput Model Eng Sci*. 2008;25(3):181-196.
45. Landers JA, Taylor RL. An augmented Lagrangian formulation for the finite element solution of contact problems. Report No. UCB/SESM-85/09, Department of Civil Engineering, University of California, Berkeley; 1985:1-21.
46. Alart P. A mixed formulation for frictional contact problems prone to Newton like solution methods. *Comput Methods Appl Mech Eng*. 1991;92:353-375.
47. Laursen JS, Laursen T. An augmented Lagrangian treatment of contact problems involving friction. *Comput Struct*. 1992;42:97-116.
48. Wriggers P. *Computational Contact Mechanics*. Springer; 2002.
49. Kikuchi N, Song YJ. Penalty finite element approximations of a class of unilateral problems in linear elasticity. *Quart Appl Math*. 1988;39(1):1-21.
50. Kikuchi N, Oden JT. *Contact Problems in Elasticity*. SIAM Publishing Company; 1988.
51. Rodríguez-Tembleque L, Abascal R, Aliabadi M. Anisotropic wear framework for 3D contact and rolling problems. *Comput Methods Appl Mech Eng*. 2012;241-244:1-19.
52. Cooper MG, Mikic BB, Yovanovich MM. Thermal contact conductance. *Int J Heat Mass Transf*. 1968;12:279-300.
53. Yovanovich MM, Culham JR, Teertstra P. Calculating interface resistance. *Electronic Cooling*. 1997;3(2):24-29.
54. Savija I, Yovanovich MM, Culham JR. Thermal joint resistance of conforming rough surfaces with grease-filled interstitial gaps. *J Thermophys Heat Transf*. 2003;17(2). doi:10.2514/2.6763
55. Yovanovich MM. Micro and macro hardness measurements, correlations, and contact models. Proceedings of the 44th AIAA Aerospace Sciences Meeting and Exhibit; 2006.
56. Alonso P. *Thermoelastic Contact Problem Using BEM*. PhD thesis. Universidad de Valladolid, Spain; 1995.
57. Rodríguez-Tembleque L, Abascal R. A FEM-BEM fast methodology for 3D frictional contact problems. *Comput Struct*. 2010;88:924-937.
58. Belhocine A, Bouchetara M. Investigation of temperature and thermal stress in ventilated disc brake based on 3D thermomechanical coupling model. *Ain Shams Eng J*. 2013;4:475-483.
59. Belhocine A, Bakar AR, Bouchetara M. Thermal and structural analysis of disc brake assembly during single stop braking event. *Austr J Mech Sci*. 2016;14(1):26-38.

**How to cite this article:** Ubero-Martínez I, Rodríguez-Tembleque L, Cifuentes-Rodríguez J, Vallepuga-Espinosa J. 3D thermoelastic solids under non-linear interface thermal and orthotropic frictional contact conditions. *Int J Numer Methods Eng*. 2022;123(11):2631-2659. doi: 10.1002/nme.6953